ARTICLE

doi:10.1038/nature14031

Three-dimensional head-direction coding in the bat brain

Arseny Finkelstein[1]*, Dori Derdikman[1,2]*, Alon Rubin[1], Jakob N. Foerster[1]†, Liora Las[1] & Nachum Ulanovsky[1]

Navigation requires a sense of direction ('compass'), which in mammals is thought to be provided by head-direction cells, neurons that discharge when the animal's head points to a specific azimuth. However, it remains unclear whether a three-dimensional (3D) compass exists in the brain. Here we conducted neural recordings in bats, mammals well-adapted to 3D spatial behaviours, and found head-direction cells tuned to azimuth, pitch or roll, or to conjunctive combinations of 3D angles, in both crawling and flying bats. Head-direction cells were organized along a functional–anatomical gradient in the presubiculum, transitioning from 2D to 3D representations. In inverted bats, the azimuth-tuning of neurons shifted by 180°, suggesting that 3D head direction is represented in azimuth × pitch toroidal coordinates. Consistent with our toroidal model, pitch-cell tuning was unimodal, circular, and continuous within the available 360° of pitch. Taken together, these results demonstrate a 3D head-direction mechanism in mammals, which could support navigation in 3D space.

Navigation requires the knowledge of one's location ('map')[1–3] and direction in space ('compass')[4,5]. The neural representation of spatial location in mammals includes place-cells which compute position[1,6–12], together with grid cells that encode distances[13–17], and border/boundary cells which indicate the edges of the environment[18–20]. The compass information is provided by head-direction cells, originally described in the rat dorsal presubiculum[21,22], which are neurons that become active whenever the animal's head points to a specific direction (azimuth) in the horizontal plane[4,15,21–28].

Orientation in 3D space is crucial for the survival of rats[29] and many other mammals that move in 3D space, including monkeys that jump across tree-tops and humans navigating through multi-storey buildings, as well as squirrels, cats, dolphins and bats[30]. Yet, it remains unknown how information about the direction of an animal in 3D is represented in the brain. Previous studies investigated the activity of place-, grid- and head-direction cells in 3D space[31–36]. However, head-direction tuning was studied primarily in planar horizontal angles (azimuth)[15,16,21–28,37] or during locomotion on planar vertical walls[32,34,38], whereas the neural representation of all 3 Euler angles of head direction has not been studied, in any species. Several pitch-sensitive cells were reported in the lateral mammillary nuclei[39] and dorsal tegmental nucleus[40] of the rat, but they responded only to upward pitch (towards the zenith), and there seemed to be no neurons encoding directions 'straight' or 'downwards'[39,40]. Moreover, neurons tuned to head roll were never found.

Finally, head-direction cells were suggested to provide the compass information that is thought to be essential for map representation in the entorhinal–hippocampal system[4,41–44]. Therefore, to elucidate the neural basis of 3D navigation and in particular, how the vertical dimension is integrated into the map representation[45], it is essential to understand the coding of 3D head direction in the brain.

Neural tuning to head azimuth, pitch, and roll

Here, we developed a custom tracking device consisting of a 3D arrangement of light-emitting diodes (LEDs), which allowed monitoring all three Euler angles of head direction in freely moving animals (Fig. 1a, b and Extended Data Fig. 1a–c; Methods). We used this device to record neural activity from the dorsal presubiculum of Egyptian fruit bats that crawled in search of food (Fig. 1b–d and Extended Data Fig. 1d–j). We conducted two behavioural sessions separated by 1 h, and analysed only neurons that showed stable directional tuning between sessions 1 and 2 ($n = 122$ directionally stable cells out of 266 total cells recorded from 4 bats; Methods). Of these 122 neurons, 78 cells (or 64%) were statistically significant head-direction cells, tuned to at least one of the three Euler angles (Methods).

We first asked whether 'classical' head-direction cells that encode azimuth are found in bat presubiculum. A large fraction of presubicular cells discharged selectively whenever the animal's head was pointing at a certain azimuth (Fig. 1e, top row). A total of $n = 63$ of the 122 cells (52%) were significantly tuned to azimuth (Methods). These azimuth-coding cells exhibited stable tuning across sessions (mean $r = 0.62$), despite their relatively low firing rates (mean peak firing rate = 1.7 Hz). The average full-tuning-width of these cells was $156^\circ \pm 6^\circ$, which was wider than that of head-direction cells in rat dorsal presubiculum[15,21] but similar to tuning-widths reported in rat lateral mammillary nuclei[39]. Despite these differences, other properties of bat azimuth-tuned cells were shared with rat head-direction cells: (i) the preferred head directions spanned all possible azimuth values across the neuronal population (Fig. 1f, top); (ii) preferred directions were maintained when the animals were moved passively by the experimenter (Extended Data Fig. 2a, b, f); (iii) head-direction cells exhibited very little place-tuning (Extended Data Fig. 3a–e); (iv) some head-direction cells were modulated by angular velocity (Extended Data Fig. 3f–h). Overall, despite the differences in firing rates and tuning widths, most properties of azimuthal head-direction cells in bats were very similar to classical head-direction cells in rats[4,21,22].

We next asked whether bat presubiculum also contained neurons tuned to pitch or roll. We found, indeed, 'pitch cells' tuned to either positive, zero or negative pitch of the head (Fig. 1e, middle), as well as 'roll cells' tuned to either right, zero or left roll of the head (Fig. 1e, bottom). Overall, 26 of the 122 cells (21%) were significantly tuned to

[1]Department of Neurobiology, Weizmann Institute of Science, Rehovot 76100, Israel. [2]Rappaport Faculty of Medicine and Research Institute, Technion – Israel Institute of Technology, Haifa 31096, Israel.
†Present address: Department of Engineering, University of Cambridge, Cambridge CB2 1PZ, UK.
*These authors contributed equally to this work.

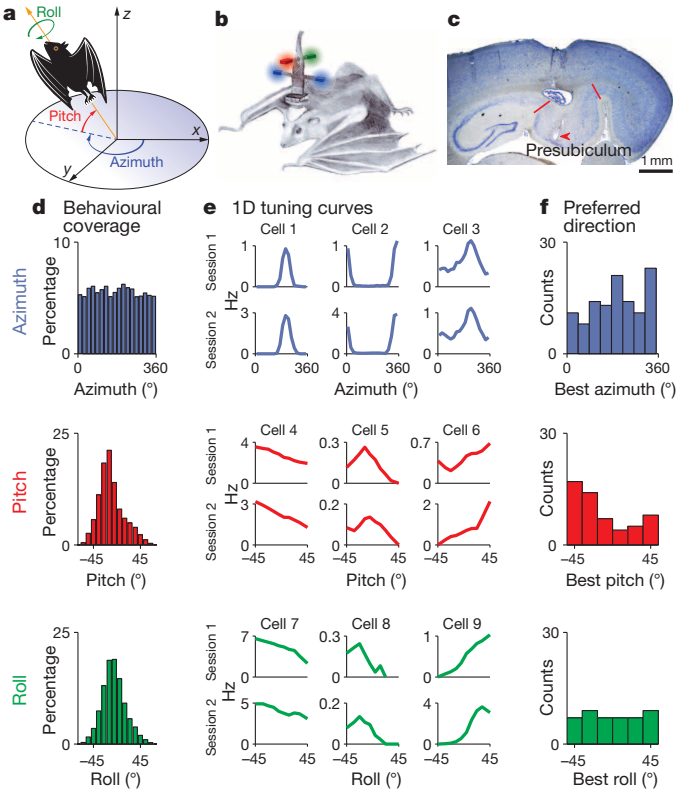

Figure 1 | Representation of head direction in the bat presubiculum: one-dimensional tuning to azimuth, pitch, and roll. **a**, Definitions of Euler angles (azimuth, pitch, roll) corresponding to the 3D rotation angles of the head. **b**, Schematic drawing of the tracking head-stage that allowed precise measurements of all 3 Euler angles of the head (see Extended Data Figs 11 and 12 and Methods for details). Illustration by S. Kaufman. **c**, Sagittal section showing tetrode track in dorsal presubiculum; arrowhead, electrolytic lesion at track end. Red lines, presubiculum borders. **d**, Behavioural distribution of head-direction angles across all upright behavioural sessions in all bats. **e**, Neural tuning curves (firing rate versus angle). Individual neurons encoded azimuth, pitch, or roll, exhibiting stable directional selectivity across behavioural sessions (rows). **f**, Preferred firing directions across the cell population span the behavioural range. Counts denote significant sessions.

pitch, and a smaller fraction, 15 cells (12%), were tuned to roll (Methods). Taken together, we identified here for the first time, to our knowledge, mammalian neurons encoding the three Euler rotation-angles of the head.

Conjunctive tuning to 3D head direction

To test whether head-direction cells encode conjunctive combinations of two Euler angles, we constructed 2D and 3D firing-rate maps in head-direction space, showing the activity of individual neurons as a function of combinations of two or three Euler angles (Fig. 2a–f). We found a diversity of directional properties in bat presubiculum neurons, including 'pure' cells tuned to only one Euler angle (Fig. 2b, c), but also many conjunctive cells that were significantly tuned to combinations of Euler angles (Fig. 2d, e; Methods). Double-conjunctive cells were quite common: of the 'classical' head-direction cells, tuned to azimuth, 27% were conjunctively tuned to pitch and 11% conjunctively tuned to roll (Fig. 2g). Triple-conjunctive neurons were rare ($n = 4$; for example, the cell in Fig. 2f, right). Thus, head direction in bat presubiculum was encoded both by neurons tuned to single Euler angles, and by multi-dimensional conjunctive neurons.

Anatomical gradient of head-direction cells

Next, we asked what is the functional–anatomical organization of head-direction cells in the dorsal presubiculum (Fig. 2h). Pure azimuth cells were very abundant in the anterior part of presubiculum, close to the subiculum, and their prevalence decreased with distance from the subiculum border, when measured along the anterior–posterior axis (Fig. 2h and Extended Data Fig. 4b; $r = -0.97$). Opposite gradients existed for pure pitch, pure roll and conjunctive cells (Extended Data Fig. 4c–e; $r > 0.7$ in all cases). Further, for the two most common cell types, pure azimuth and conjunctive cells, we found that their abundances followed in fact a diagonal gradient along the transverse axis of dorsal presubiculum, with pure azimuth cells being most common in the antero–lateral (proximal) part of presubiculum and conjunctive cells in the postero–medial (distal) part (Fig. 2i and Extended Data Fig. 4g–o). This striking functional gradient (Fig. 2i) raises the possibility that proximal presubiculum is used mostly for planar 2D orientation, whereas the distal presubiculum may be involved in orientation in 3D.

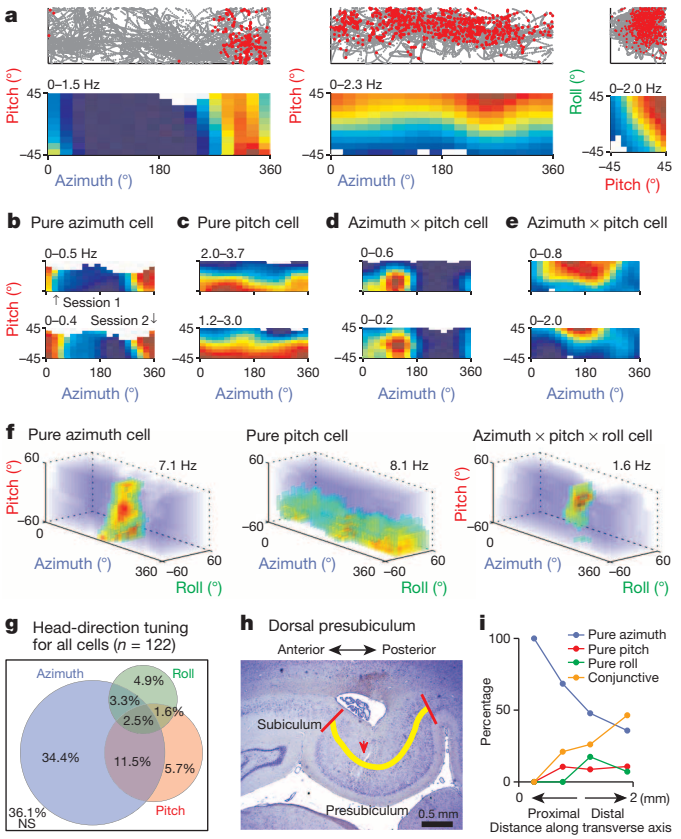

Figure 2 | Single cells encode one, two, or three Euler angles of head direction, and are organized according to a functional–anatomical gradient. **a**, Example cells. Raw data (top; grey line, head direction; red dots, spikes), and corresponding 2D colour-coded rate-maps (bottom), showing the directional field for 3 neurons in 2D projections (pitch × azimuth and roll × pitch). The range of pitch and roll in the 2D plots was limited to match the behavioural range of angles covered by the bats (Fig. 1d). **b**–**e**, Examples of 4 neurons with different tuning properties, showing the 2D rate-maps for the two sessions (rows); minimal and maximal firing rates (in Hz) are indicated. **f**, Firing-rate maps in 3D projections (azimuth × pitch × roll) for a pure azimuth cell (left), pure pitch cell (middle), and triple-conjunctive cell tuned to all 3 Euler angles (right). **g**, Proportions of functional cell types in bat presubiculum (Methods). **h**, **i**, Functional–anatomical gradient of head-direction cells in dorsal presubiculum. **h**, Sagittal section through presubiculum; red lines, presubiculum borders. Yellow line: axis used to determine the anterior–posterior distance of the tetrode-track (arrowhead) from the subiculum border. **i**, Percentages of cells with pure tuning to azimuth, pitch, or roll, and conjunctive neurons tuned to any angular combination, plotted versus the recording position along the presubiculum's transverse axis (Methods; graph based on all significant head-direction cells, $n = 78$; the four positional bins contain 8, 19, 23, 28 cells).

Azimuth tuning in inverted bats shifts by 180°

We next asked, what coordinate system is used by the brain to represent 3D head direction. The direction of a vector in 3D space is defined by azimuth and pitch, whereas roll is merely a rotation around this axis. As bats were shown to manoeuvre mostly in azimuth and pitch and much less in roll (ref. 46; see also Supplementary Video 1), and because conjunctive tuning to roll was relatively rare (Fig. 2g), we focused on azimuth and pitch. One way to dissociate between possible coordinate frames for representing azimuth × pitch is to invert the animal, which is also ethologically relevant for bats.

We therefore introduced an inverted session (flanked between the two upright sessions), and found that nearly half of the azimuth-selective cells retained a directional firing when the bat was passively moved upside-down (Fig. 3a, middle row, blue lines; and Extended Data Fig. 5). Surprisingly, the cells' best tuning-angle in azimuth was shifted by 180°, relative to the best tuning angle in upright sessions 1 and 2 (Fig. 3a, middle row, magenta lines show 180°-shifted tuning curves; compare to the top and bottom rows). The 180°-shift was evident also at the population level: the differences in preferred azimuth between the two upright sessions were distributed around zero, indicating stability (Fig. 3b, top), whereas the differences between the upright and inverted sessions had a U-shaped distribution, peaking at ± 180° (Fig. 3b, bottom and Extended Data Fig. 5d). Notably, the 180°-shift in the preferred azimuth of the neurons in inverted bats, was not caused by the fact that the inverted bat was moved passively (because passive-upright and active-upright tuning was very similar: see Extended Data Fig. 2a, b, f). The 180°-shift was also observed when bats had positioned themselves upside-down of their own volition (Extended Data Fig. 6). Interestingly, these results are different from findings in inverted rats, where many head-direction cells were reported to lose their directional properties[33,34].

Toroidal model of 3D head–direction cells

If head-direction cells simply encode the bearing of a vector in 3D space (which can be described in spherical coordinates, Fig. 3c), the neurons are expected to fire whenever the bat's head is directed towards the same distal point, irrespective of whether the bat is upright or inverted (Extended Data Fig. 7a, b). Our results of 180°-shift in the preferred direction under inversion, suggest that head direction in the bat presubiculum is not represented in spherical coordinates. Instead, it could be modelled by a toroidal manifold consisting of two independent cyclical degrees of freedom, 360° azimuth and 360° pitch (Fig. 3d, and Extended Data Fig. 7c, d). According to this model, pitching the head beyond ± 90°, does not change the azimuth angle in toroidal coordinates (Fig. 3d, red ring), and therefore a neuron tuned to a certain azimuth should keep firing also in the inverted position when the bat faces the 180°-opposite direction, as indeed we observed (Fig. 3a, b). Comparison of the correlations between upright and inverted sessions, computed in spherical versus toroidal coordinates, showed significantly higher correlations for the toroidal representation (Fig. 3e; *t*-test: $P < 0.001$; Methods).

Further, the toroidal representation entails that pure azimuth cells should appear as a vertical band on the torus (Fig. 3f, left column); pure pitch cells should form a horizontal band (Fig. 3f, middle); whereas conjunctive azimuth × pitch cells should appear as a patch (Fig. 3f, right). This was indeed found for all three cell types (Fig. 3f, and Extended Data Figs 7 and 8).

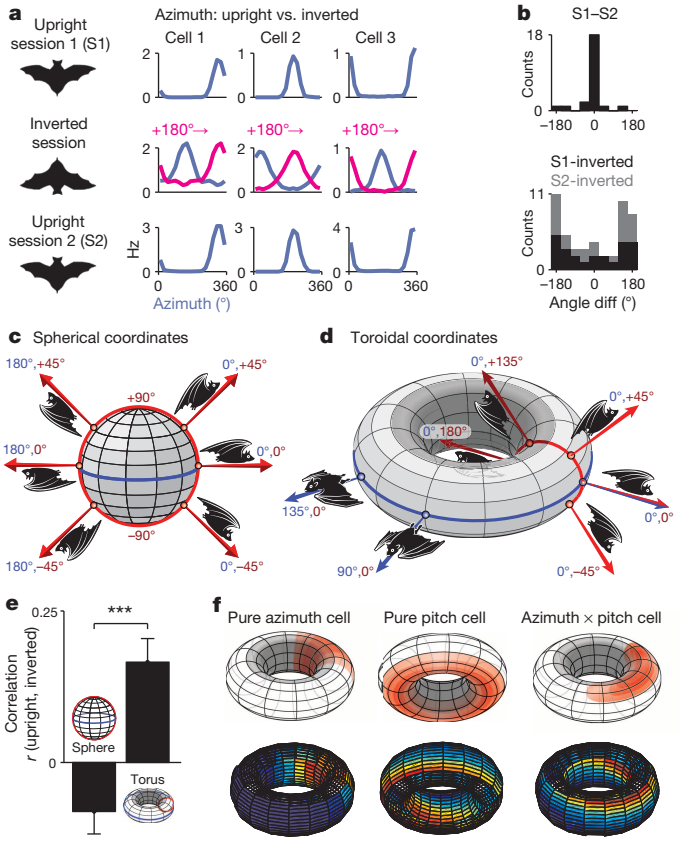

Figure 3 | Azimuth tuning in inverted bats is consistent with a toroidal model of head-direction coding. **a**, Azimuth tuning in three example cells, across the two upright behavioural sessions (top and bottom rows) and the inverted session (middle row, blue). Magenta curves in middle row: tuning-curves of the inverted session, shifted by 180°. **b**, Distributions of differences in preferred direction between sessions, for cells significantly tuned to azimuth in the inverted session. Top, angular difference between the two upright behavioural sessions (S1–S2), showing a peak in the distribution near 0 °, indicating stability. Bottom, angular difference between each of the upright sessions and the inverted session (S1-inverted, S2-inverted), indicating 180°-shift of the preferred direction in the inverted session. **c**, Schematic depiction of azimuth (blue) and pitch (red) in spherical coordinates. Numerical values of azimuth and pitch are indicated with corresponding colours. Pitching beyond ± 90° (along the red circle) results in abrupt shift of head azimuth by 180°. **d**, Toroidal coordinates, in which for each azimuth (blue) there is a 360° range of possible pitch-angles (red). Outer surface of the torus corresponds to upright bat positions; inner surface, to inverted positions. All positions along the red circle (corresponding to pitch angles between ± 180°) keep the same azimuth in the toroidal coordinates, hence pitching beyond ± 90° does not change the azimuth (contrary to spherical coordinates, red circle in **c**). See also Extended Data Fig. 7a–d. **e**, Average 2D-correlations of firing maps in upright versus inverted sessions, for all cells tuned to azimuth or pitch ($n = 144$ (72 cells × 2 sessions)), represented in either spherical (left) or toroidal coordinates (right). Error bars, mean ± s.e.m.; ***$P < 0.001$. **f**, Toroidal 2D head-direction fields for a pure azimuth cell (left), pure pitch cell (middle), and conjunctive azimuth × pitch cell (right). Upper panels, schematic illustrations. Lower panels, 3 example neurons; transparent bins, angles where the animal spent < 0.5 s.

Pitch cells exhibit circular tuning to 360°

The toroidal model implies that pitch is represented allocentrically and continuously over a circular range of 360° (Fig. 3d and Extended Data Fig. 9). To directly test this prediction, we recorded 175 cells from the presubiculum of 2 additional bats that crawled inside a vertical ring (Fig. 4a, pose 2). Pitch cells exhibited clear tuning (Fig. 4b, red curves, and Extended Data Fig. 10b, c), and the preferred pitch angles for different neurons were distributed across the entire 360° circular range of pitch, with a slight over-representation of 0 ° pitch (Fig. 4c; χ^2 test for non-uniformity: $P < 0.01$). The 'ramp-like' tuning often observed on the arena floor (Fig. 4b, black, corresponding to Fig. 4a, 'pose 1') was in fact a clipped version of the full circular tuning on the ring (Fig. 4b, compare black to red curves; population data, Fig. 4d). Similar to azimuth cells, individual pitch cells exhibited unimodal tuning (Fig. 4b, e, f and Extended Data Fig. 10b, c). Tuning widths for pitch cells were quite similar to those of azimuth cells (Fig. 4g and Extended Data Fig. 10). We thus conclude that the tuning to pitch was circular (360°), unimodal, and continuous.

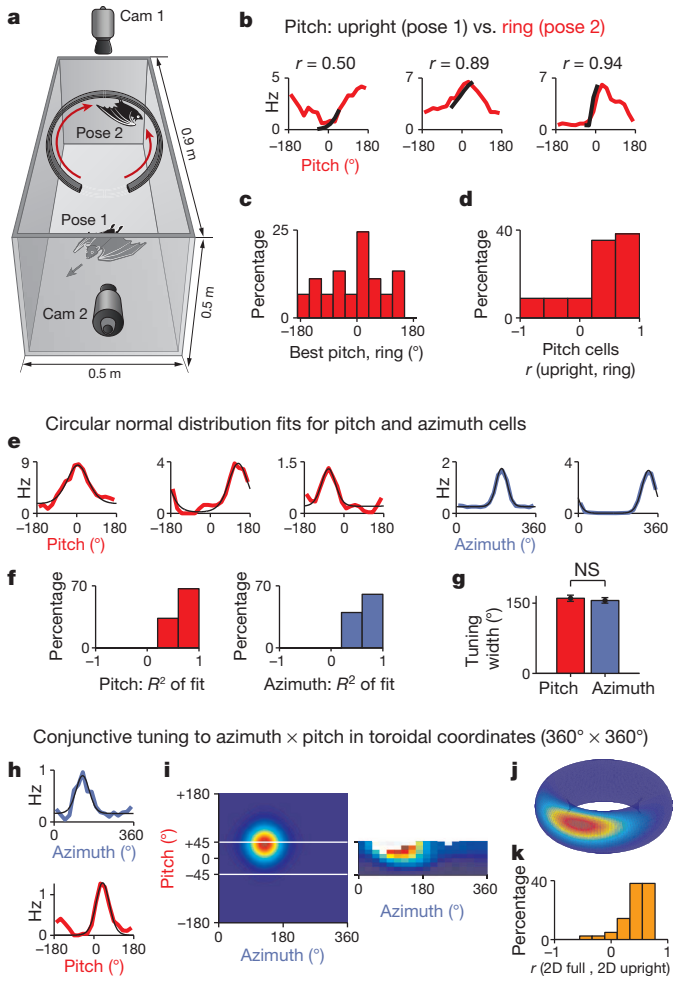

Figure 4 | Pitch cells are tuned unimodally and continuously to a cyclical range of 360°, as predicted by the toroidal model. **a**, Behavioural setup number 2 allowed a comparison of head-direction tuning when the bat crawled on the arena floor ('pose 1') versus crawling along the inner side of a vertically positioned ring ('pose 2'). **b**, Pitch tuning of 3 example cells during ring locomotion (red curve, pose 2, ranging between ± 180°), overlaid on the pitch tuning of the same neurons during floor locomotion (black curve, pose 1, ranging between ± 45°). **c**, Distribution of preferred firing directions of pitch-significant cells on the ring ($n = 45$); note that the population spans the full range of 360°. **d**, Distribution of correlation-coefficients for pitch tuning on ring versus floor. **e**, Examples of pitch and azimuth cells (red and blue curves, respectively), fitted with von Mises circular normal functions (black curves). **f**, Distributions of R^2 values of von Mises fits to pitch and azimuth. **g**, Average tuning width was similar for azimuth cells and pitch cells. Error bars, mean ± s.e.m. **h**, Example of a conjunctive cell tuned to azimuth (top) and pitch (bottom), overlaid with von Mises fits (black curves). **i**, Left, full 360° × 360° fitted 2D rate-map for the neuron in **h**, computed by multiplying the 1D von Mises fits to azimuth and pitch. Right, actual 2D rate map measured for this neuron during floor locomotion (the pitch range sampled on the floor is indicated by white lines on the left panel). **j**, Same 360° × 360° fitted map as in **i**, presented in toroidal coordinates by wrapping the full 2D directional map around both axes. **k**, Distribution of correlation coefficients between the 2D map measured on the floor (as in **i**, right panel) and the relevant range of the full 2D map (as in **i**, left panel, the segment between the white lines), plotted for all the pitch and azimuth cells with sufficient number of spikes on both floor and ring ($n = 42$; Methods). NS, not significant.

Further, reconstruction of the full 360° × 360° unwrapped maps for conjunctive azimuth × pitch neurons, matched closely the actual receptive fields observed on the floor of the arena (Fig. 4h–k), as predicted by the toroidal model. Taken together, these results suggest a torus-based representation of 3D head direction in the bat presubiculum.

Head-direction cells in freely flying bats

An intriguing question is whether the 3D head-direction tuning that we observed in crawling bats would also be found during flight, where the movement is volumetric and not anchored to a specific locomotion plane. To test this, we used a wireless device to record 67 cells from the dorsal presubiculum during flight (Fig. 5a). We found that 30% of the cells ($n = 20/67$) were significantly directionally tuned, a very similar proportion to the 29% (78/266) found in crawling bats. Moreover, similar to crawling bats, the flight data revealed pure azimuth, pure pitch, and conjunctive azimuth × pitch neurons (Fig. 5b). Tuning widths were also similar between flight and crawling (Fig. 5c). Interestingly, peak firing rates were more than twofold higher in flight as compared to crawling (Fig. 5d), consistent with the increased linear and angular velocity during flight[36]. Collectively, these data suggest the existence of 3D head-direction tuning in both crawling and flight.

Discussion

Here we present the first evidence, to our knowledge, for a conjunctive representation of 3D head direction in the mammalian brain (Figs 1 and 2), which may serve as a '3D neural compass'. Head-direction cells were organized along the transverse axes of the presubiculum, with pure azimuth ('2D') cells being more prevalent in its proximal part and conjunctive 3D cells more abundant distally (Fig. 2h, i). Tuning widths for azimuth and pitch were rather similar (Fig. 4g). Notably, we found a surprising 180°-shift of the preferred-azimuth direction in inverted bats (Fig. 3), and a cyclical tuning of pitch cells to 360°-pitch (Fig. 4). These results, together with our finding of conjunctive cells, suggested that head direction is represented in toroidal coordinates (azimuth × pitch).

The 3D head-direction cells described here, together with the 3D place-cells that we recently found in the bat hippocampus[36], could support 3D 'map-and-compass' navigation. We predict that conjunctive 3D head-direction cells might be found also in non-flying mammals that move in complex 3D environments or that orient their head up/down, such as squirrels, cats, dolphins and primates. Of particular interest will be to record from the presubiculum of mice which, in contrast to rats, naturally hang and locomote upside-down very well. We expect

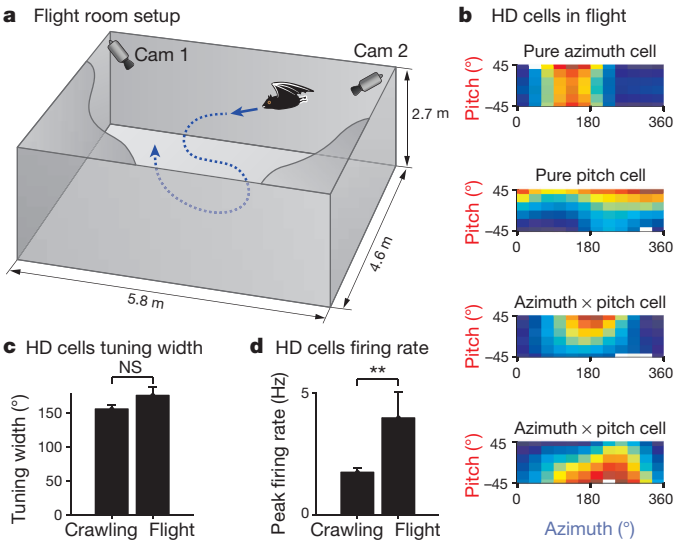

Figure 5 | Head-direction cells in freely flying bats. **a**, Behavioural setup number 3: flight-room. Objects and cues located in the room were omitted from the schematic, for clarity. **b**, Examples showing 2D rate-maps of head-direction cells recorded in flight, exhibiting different tuning properties: a pure azimuth cell, a pure pitch cell, and two azimuth × pitch cells. **c**, Average tuning width for azimuth cells recorded during crawling ($n = 63$) and in flight ($n = 14$). Error bars, mean ± s.e.m. **d**, Average peak firing rate for all the significant head-direction cells in crawling ($n = 78$) versus flight ($n = 20$). Firing rates increased more than twofold during flight. Error bars, mean ± s.e.m.; $^{**}P < 0.01$. HD, head direction.

that, under inversion, head-direction cells in mice will exhibit similar properties to those in bats.

Our results yield interesting predictions for 3D grid cells. Proximal presubiculum (containing 2D head-direction cells, Fig. 2h, i) is known to project to distal medial entorhinal cortex (MEC), whereas distal presubiculum (containing 3D head-direction cells) projects to proximal MEC[47]. Because computational models propose that head-direction information is used for path-integration to form grid cells[43,48], we might expect a gradient of 2D-to-3D grid cells in flying bats—that is, 2D grid cells (vertical columns) in distal MEC, near the border with lateral entorhinal cortex; and 3D grids (for example, 3D close-packing of spheres) in proximal MEC, near the border with parasubiculum.

The proposed toroidal model of head-direction coding is a generalization of the hemi-torus model for rat head-direction cells[32], extended to the inverted pose. A fully toroidal topology has several advantages. First, it avoids undesirable network instabilities. In the spherical coordinate system, rotation of the head beyond $\pm 90^\circ$ pitch will result in an abrupt shift of the azimuth by 180°, and hence in abrupt changes of ensemble neural activity. In contrast, the toroidal topology confers continuity and stability, thus avoiding singularities in network activity when the bat passes through $\pm 90^\circ$ of pitch (see Supplementary Video 1 for example passages through $\pm 90^\circ$ of pitch). Second, an allocentric toroidal representation is commutative. Finally, a toroidal topology could directly support toroidal continuous attractor network models of head direction[48–50].

The torus is not necessarily the only possible model that can explain our data. The full set of rotations in 3D is described by 'real projective space 3' (RP^3, also known as 'hypersphere of rotations'), which has three degrees of freedom (azimuth, pitch, and roll), whereas the torus is a manifold within RP^3, with only two degrees of freedom (azimuth $\times$ pitch). However, for animals like bats—which exhibit very little roll, but manoeuvre substantially in azimuth and pitch—the torus is the simplest low-dimensional manifold within RP^3 that is consistent with our data.

Finally, we note that head-azimuth was defined to date as the direction of the animal's nose (rostro–caudal axis) in the horizontal plane; however, the toroidal representation can be naturally interpreted as a coordinate system with two orthogonal axes: the azimuthal direction is anchored to the interaural axis (the animal's ears), and thus remains the same for any pitch, whereas the pitch direction is being anchored to the rostro–caudal axis.

In summary, the toroidal topology of 3D head-direction representation in bats is consistent with the animal's natural behaviour and the need to represent absolute 3D directions in space, as well as with biological requirements for network stability, and with the structure of continuous attractor models. Thus, it provides a convergence of ethology, neurobiology and computation.

Online Content Methods, along with any additional Extended Data display items and Source Data, are available in the online version of the paper; references unique to these sections appear only in the online paper.

Received 25 July; accepted 4 November 2014.

Published online 3 December 2014.

1. O'Keefe, J. & Nadel, L. *The Hippocampus as a Cognitive Map* (Oxford Univ. Press, 1978).
2. Gallistel, C. R. *The Organization of Learning* (MIT Press, 1990).
3. Menzel, R. *et al.* Honey bees navigate according to a map-like spatial memory. *Proc. Natl Acad. Sci. USA* **102,** 3040–3045 (2005).
4. Taube, J. S. The head direction signal: origins and sensory-motor integration. *Annu. Rev. Neurosci.* **30,** 181–207 (2007).
5. Wu, L. Q. & Dickman, J. D. Neural correlates of a magnetic sense. *Science* **336,** 1054–1057 (2012).
6. O'Keefe, J. & Dostrovsky, J. The hippocampus as a spatial map. Preliminary evidence from unit activity in the freely-moving rat. *Brain Res.* **34,** 171–175 (1971).
7. Wilson, M. A. & McNaughton, B. L. Dynamics of the hippocampal ensemble code for space. *Science* **261,** 1055–1058 (1993).
8. Leutgeb, S. *et al.* Independent codes for spatial and episodic memory in hippocampal neuronal ensembles. *Science* **309,** 619–623 (2005).
9. Ulanovsky, N. & Moss, C. F. Hippocampal cellular and network activity in freely moving echolocating bats. *Nature Neurosci.* **10,** 224–233 (2007).
10. Harvey, C. D., Collman, F., Dombeck, D. A. & Tank, D. W. Intracellular dynamics of hippocampal place cells during virtual navigation. *Nature* **461,** 941–946 (2009).
11. Royer, S. *et al.* Control of timing, rate and bursts of hippocampal place cells by dendritic and somatic inhibition. *Nature Neurosci.* **15,** 769–775 (2012).
12. Miller, J. F. *et al.* Neural activity in human hippocampal formation reveals the spatial context of retrieved memories. *Science* **342,** 1111–1114 (2013).
13. Hafting, T., Fyhn, M., Molden, S., Moser, M.-B. & Moser, E. I. Microstructure of a spatial map in the entorhinal cortex. *Nature* **436,** 801–806 (2005).
14. Barry, C., Hayman, R., Burgess, N. & Jeffery, K. J. Experience-dependent rescaling of entorhinal grids. *Nature Neurosci.* **10,** 682–684 (2007).
15. Boccara, C. N. *et al.* Grid cells in pre- and parasubiculum. *Nature Neurosci.* **13,** 987–994 (2010).
16. Yartsev, M. M., Witter, M. P. & Ulanovsky, N. Grid cells without theta oscillations in the entorhinal cortex of bats. *Nature* **479,** 103–107 (2011).
17. Jacobs, J. *et al.* Direct recordings of grid-like neuronal activity in human spatial navigation. *Nature Neurosci.* **16,** 1188–1190 (2013).
18. Solstad, T., Boccara, C. N., Kropff, E., Moser, M.-B. & Moser, E. I. Representation of geometric borders in the entorhinal cortex. *Science* **322,** 1865–1868 (2008).
19. Savelli, F., Yoganarasimha, D. & Knierim, J. J. Influence of boundary removal on the spatial representations of the medial entorhinal cortex. *Hippocampus* **18,** 1270–1282 (2008).
20. Lever, C., Burton, S., Jeewajee, A., O'Keefe, J. & Burgess, N. Boundary vector cells in the subiculum of the hippocampal formation. *J. Neurosci.* **29,** 9771–9777 (2009).
21. Taube, J. S., Muller, R. U. & Ranck, J. B. Jr. Head-direction cells recorded from the postsubiculum in freely moving rats. I. Description and quantitative analysis. *J. Neurosci.* **10,** 420–435 (1990).
22. Taube, J. S., Muller, R. U. & Ranck, J. B. Jr. Head-direction cells recorded from the postsubiculum in freely moving rats. II. Effects of environmental manipulations. *J. Neurosci.* **10,** 436–447 (1990).
23. Zugaro, M. B., Berthoz, A. & Wiener, S. I. Background, but not foreground, spatial cues are taken as references for head direction responses by rat anterodorsal thalamus neurons. *J. Neurosci.* **21,** RC154 (2001).
24. Sargolini, F. *et al.* Conjunctive representation of position, direction, and velocity in entorhinal cortex. *Science* **312,** 758–762 (2006).
25. Langston, R. F. *et al.* Development of the spatial representation system in the rat. *Science* **328,** 1576–1580 (2010).
26. Wills, T. J., Cacucci, F., Burgess, N. & O'Keefe, J. Development of the hippocampal cognitive map in preweanling rats. *Science* **328,** 1573–1576 (2010).
27. Valerio, S. & Taube, J. S. Path integration: how the head direction signal maintains and corrects spatial orientation. *Nature Neurosci.* **15,** 1445–1453 (2012).
28. Brandon, M. P., Bogaard, A. R., Schultheiss, N. W. & Hasselmo, M. E. Segregation of cortical head direction cell assemblies on alternating theta cycles. *Nature Neurosci.* **16,** 739–748 (2013).
29. Wallace, D. J. *et al.* Rats maintain an overhead binocular field at the expense of constant fusion. *Nature* **498,** 65–69 (2013).
30. Yovel, Y., Falk, B., Moss, C. F. & Ulanovsky, N. Optimal localization by pointing off axis. *Science* **327,** 701–704 (2010).
31. Knierim, J. J., McNaughton, B. L. & Poe, G. R. Three-dimensional spatial selectivity of hippocampal neurons during space flight. *Nature Neurosci.* **3,** 209–210 (2000).
32. Stackman, R. W., Tullman, M. L. & Taube, J. S. Maintenance of rat head direction cell firing during locomotion in the vertical plane. *J. Neurophysiol.* **83,** 393–405 (2000).
33. Taube, J. S., Stackman, R. W., Calton, J. L. & Oman, C. M. Rat head direction cell responses in zero-gravity parabolic flight. *J. Neurophysiol.* **92,** 2887–2997 (2004).
34. Calton, J. L. & Taube, J. S. Degradation of head direction cell activity during inverted locomotion. *J. Neurosci.* **25,** 2420–2428 (2005).
35. Hayman, R., Verriotis, M. A., Jovalekic, A., Fenton, A. A. & Jeffery, K. J. Anisotropic encoding of three-dimensional space by place cells and grid cells. *Nature Neurosci.* **14,** 1182–1188 (2011).
36. Yartsev, M. M. & Ulanovsky, N. Representation of three-dimensional space in the hippocampus of flying bats. *Science* **340,** 367–372 (2013).
37. Rubin, A., Yartsev, M. M. & Ulanovsky, N. Encoding of head direction by hippocampal place cells in bats. *J. Neurosci.* **34,** 1067–1080 (2014).
38. Taube, J. S., Wang, S. S., Kim, S. Y. & Frohardt, R. J. Updating of the spatial reference frame of head direction cells in response to locomotion in the vertical plane. *J. Neurophysiol.* **109,** 873–888 (2013).
39. Stackman, R. W. & Taube, J. S. Firing properties of rat lateral mammillary single units: head direction, head pitch, and angular head velocity. *J. Neurosci.* **18,** 9020–9037 (1998).
40. Bassett, J. P. & Taube, J. S. Neural correlates for angular head velocity in the rat dorsal tegmental nucleus. *J. Neurosci.* **21,** 5740–5751 (2001).
41. Calton, J. L. *et al.* Hippocampal place cell instability after lesions of the head direction cell network. *J. Neurosci.* **23,** 9719–9731 (2003).
42. Bonnevie, T. *et al.* Grid cells require excitatory drive from the hippocampus. *Nature Neurosci.* **16,** 309–317 (2013).
43. Burak, Y. & Fiete, I. R. Accurate path integration in continuous attractor network models of grid cells. *PLoS Comput. Biol.* **5,** e1000291 (2009).
44. Canto, C. B., Koganezawa, N., Beed, P., Moser, E. I. & Witter, M. P. All layers of medial entorhinal cortex receive presubicular and parasubicular inputs. *J. Neurosci.* **32,** 17620–17631 (2012).
45. Jeffery, K. J., Jovalekic, A., Verriotis, M. & Hayman, R. Navigating in a three-dimensional world. *Behav. Brain Sci.* **36,** 523–543 (2013).
46. Iriarte-Díaz, J. & Swartz, S. M. Kinematics of slow turn maneuvering in the fruit bat *Cynopterus brachyotis*. *J. Exp. Biol.* **211,** 3478–3489 (2008).

47. Honda, Y. & Ishizuka, N. Organization of connectivity of the rat presubiculum: I. Efferent projections to the medial entorhinal cortex. *J. Comp. Neurol.* **473,** 463–484 (2004).
48. McNaughton, B. L., Battaglia, F. P., Jensen, O., Moser, E. I. & Moser, M.-B. Path integration and the neural basis of the 'cognitive map'. *Nature Rev. Neurosci.* **7,** 663–678 (2006).
49. Zhang, K. Representation of spatial orientation by the intrinsic dynamics of the head-direction cell ensemble: a theory. *J. Neurosci.* **16,** 2112–2126 (1996).
50. Redish, A. D., Elga, A. N. & Touretzky, D. S. A coupled attractor model of the rodent head direction system. *Network Comput. Neural Sys.* **7,** 671–685 (1996).

Supplementary Information is available in the online version of the paper.

Acknowledgements We thank A. Treves, J.-M. Fellous, M. Okun, A. Wallach, M. Geva-Sagiv and M. M. Yartsev for comments on the manuscript; B. Pasmantirer and G. Ankaoua for mechanical designs; S. Kaufman for bat training, assistance in neural recordings, and illustrations; T. Eliav and T. Tamir for help in experiments; A. Tuval and M. Weinberg for veterinary oversight; G. Brodsky for graphics; R. Eilam and C. Ra'anan for histology; and M. P. Witter for advice on reconstruction of tetrode-track locations and anatomical delineations. This study was supported by research grants to N.U. from the European Research Council (ERC–NEUROBAT), the Human Frontiers Science Program (HFSP RGP0062/2009-C), the Israel Science Foundation (ISF 1017/08 and ISF 1319/13), and the Minerva Foundation; by a Clore predoctoral excellence fellowship to A.F.; and by an MIT-Israel (MISTI) student exchange internship to J.N.F. D.D. is the incumbent of the David and Inez Myers Career Advancement Chair in Life Sciences.

Author Contributions A.F., D.D. and N.U. designed the experiments and the analyses. A.F. performed the experiments, with contributions by D.D. and L.L. to some of the surgeries and tetrode recordings. A.F. and A.R. developed the toroidal model. A.F. and J.N.F. developed algorithms. A.F. analysed the data, and discussed with D.D, A.R., L.L. and N.U. the results and interpretations. A.F. and N.U. wrote the manuscript with input from D.D., A.R., J.N.F. and L.L.

Author Information Reprints and permissions information is available at www.nature.com/reprints. The authors declare no competing financial interests. Readers are welcome to comment on the online version of the paper. Correspondence and requests for materials should be addressed to N.U. (nachum.ulanovsky@weizmann.ac.il).

METHODS

Subjects and behavioural training. Neural recording experiments were conducted in 3 different behavioural setups: (i) upright-crawling arena ($n = 4$ bats), (ii) vertical-ring arena ($n = 2$ bats), and (iii) flight room ($n = 1$ bat). All experiments were conducted in adult male Egyptian fruit bats, *Rousettus aegyptiacus* (weight 139–176 g at implantation). Bats were maintained on a reversed light/dark cycle; experiments were carried out in the dark phase. All experimental procedures were approved by the Institutional Animal Care and Use Committee of the Weizmann Institute of Science.

For the set of experiments conducted in crawling bats in setup number 1 (Figs 1–3), neural activity was recorded from the dorsal presubiculum of 4 bats, as they crawled in a square (50 × 50 cm) wooden box that was used throughout the training and recording period (Extended Data Fig. 1a). The square arena had 50-cm high walls, its floor and walls were coloured in black, and a portion of one of the walls was painted white and served as a polarizing cue (18-cm wide × 50-cm high white cue card). The arena was placed horizontally on the floor of a large room; the position of the arena within the room was fixed throughout the duration of training and testing, and the locations of its four corners were calibrated periodically. Bats were trained to crawl on the arena floor that was covered with a soft rubber surface, in search for randomly scattered food (pieces of fruit: bananas or dates). During this random foraging task bats moved their head extensively in 3D, in azimuth, pitch, and roll (see Fig. 1d). All training and recording sessions were done under low-light conditions (illuminance 1 lx; measured using ILT-1700 illuminance meter, International Light, MA), a light level that allows these highly visual bats[51,52] to clearly use vision.

The sequence of behavioural recording sessions was typically flanked by sleep sessions, during which the bat was comfortably placed inside a holding bag, with its head and neck outside the bag, and rested on a pedestal inside the experimental room. The full sequence of sessions was as follows: sleep, upright session 1, inverted session, upright passive session, upright session 2, sleep. Sleep sessions lasted ~10 min each, while the behavioural sessions lasted 15–25 min each. The total duration of the crawling experiment was ~2 h. In the 'upright sessions' the bat was required to crawl in the arena in search for randomly delivered food. In the 'inverted session' the bat was loosely held by the experimenter in a holding-bag and was moved above the arena with its head upside-down; while in the bag, the animal was free to move its head all around. In the 'passive session' the bat was placed in an upright position in the holding-bag, and was moved by the experimenter over the floor of the arena. Throughout the duration of the daily recordings, the bats were not taken outside of the recording room.

For the experiments in setup number 2, with bats crawling on a ring, we built a 90 × 50 cm box containing a vertically oriented ring, positioned 25 cm from the short wall of the box (Fig. 4a), and trained 2 bats to either crawl on the floor as before (Fig. 4a, pose 1), or climb onto the inner surface of the ring and complete a full 360° revolution (360° pitch angles; Fig. 4a, pose 2). The ring (50-cm diameter × 8-cm width) was made from plastic mesh with 0.8 × 0.8 cm holes, which allowed the bat to cling to it and crawl along its inner surface. Importantly, we trained the bats to crawl in the same session both on the arena floor and on the vertical ring, so that the ring traversal was done of the bat's own volition, and was intermingled with crawling on the arena floor. This design allowed comparing the neural activity during upright crawling on the arena floor, which had a limited range of pitch coverage (approximately ± 45°), with the activity on the ring, where behavioural sampling covered all possible pitch angles (360° pitch). In total, each session lasted for 30–45 min, with the bat spending roughly half of the time on the arena floor and half of the time on the ring. The recording session was flanked by two sleep sessions, lasting 10 min each.

For the flight experiments in setup number 3, one bat was trained to fly in a large flight-room (5.8 × 4.6 × 2.7 m; Fig. 5a) in search for randomly positioned food rewards (banana pieces). The flight room contained multiple objects, on which the reward was randomly placed. These objects included elevated poles and hanging balls, and the variety of objects and positions allowed for a maximal diversification of the flight trajectories, in order to produce sufficient coverage of the z axis and of all possible 3D directions. The recording session in the flight experiments typically lasted 45–60 min, and was flanked by two sleep sessions, lasting 10 min each.

No statistical method was used to predetermine sample size.

Surgery and recording techniques. All surgical and recording procedures were as described previously[16]. Briefly, after completion of training, bats were implanted with a four-tetrode lightweight microdrive (4-drive, Neuralynx; weight 2.1 g). Tetrodes (~45 μm diameter) were constructed from four strands of platinum-iridium wire (17.8 μm diameter, HML-insulated), bound together by twisting and melting their insulations; tetrode wires were gold-plated on the day before surgery to reduce their impedance to 300–700 kΩ. While the bat was under isoflurane anaesthesia, a circular opening (craniotomy of 1.8-mm diameter) was made in the skull over the right hemisphere. The centre of craniotomy was positioned over the dorsal presubiculum, 3.3 mm lateral to the midline and 3.15 mm anterior to the transverse sinus that runs between the posterior part of the cortex and the cerebellum (N. Ulanovsky, M. P. Witter and R. Eilam, *Stereotaxic Brain Atlas of the Egyptian Fruit Bat*, in preparation).

Following surgery, tetrodes were slowly lowered towards the presubiculum. The precise positioning of each tetrode was later reconstructed histologically (see below). The tetrodes were always moved at the end of each recording day (40–200 μm daily), in order to obtain recordings from new ensembles of neurons daily. For each bat, one tetrode was left in an electrically quiet zone and served as a reference, and the remaining three tetrodes served as recording probes. During recordings in crawling bats, a unity-gain preamplifier (HS-18, Neuralynx) was attached to a connector on the microdrive. Signals were amplified (× 1,400–5,000) and band-pass filtered (600–6,000 Hz, Lynx-8 or DigitalLynx, Neuralynx), and a voltage-threshold was used for collecting 1-ms spike waveforms, sampled at 32 kHz. For flight experiments, we used a wireless neural-recording device (an improved version of the device described in ref. 36). In all setups, data were collected continuously throughout all the behavioural and sleep sessions of each recording day (1.5–2 h daily).

Video recordings and reconstruction of 3D head-direction angles. In order to reconstruct the 3D head direction of the bat as it was crawling in setup number 1 (Extended Data Fig. 1a), using the 2D tracking data of a single camera, we added a custom 3D tetrahedral arrangement of four LEDs to the recording head-stage on the bat's head (illustrated in Extended Data Figs 1b, c and 11). The positions of these LEDs were recorded using a single camera that was placed vertically overhead the arena, and was connected to a video-tracker (Neuralynx) with a 25-Hz sampling rate, which was synchronized to the neural recordings. Combined with the data-analysis algorithm described below, this LED arrangement enabled a precise mapping from the position of these four LEDs in the camera image, onto a complete set of coordinates describing the five degrees of freedom of the bat's head. These degrees of freedom include the two spatial coordinates (x, y) for the position inside the arena, and three Euler angles describing the head rotation: yaw ('azimuth', φ), pitch (θ), and roll (γ). For more details, see Extended Data Figs 11 and 12 and the last section of the Methods, which describes the algorithm for reconstructing the 3D head direction.

In the ring apparatus (setup number 2: Fig. 4a), when the bat crawled on the floor in the upright position (Fig. 4a, pose 1), the 3D head direction was measured using the video data acquired from the overhead camera (Fig. 4a, 'cam 1'), as described above for setup number 1. When the bat crawled on the inside part of the ring (Fig. 4a, pose 2), we used instead a second camera pointing horizontally (Fig. 4a, 'cam2') to measure the pitch (θ) of the bat's head over the entire 360° of possible pitch angles, based on the red–green LED pair. In addition, we used the horizontally pointing camera to determine whether the bat performed a ring traverse in the eastbound or westbound direction (see Extended Data Fig. 6).

In the flight apparatus (setup number 3: Fig. 5a), we estimated the head direction of the bat by taking advantage of a previous finding that in flying Egyptian fruit bats, heading-direction (flight direction) is tightly coupled to head direction during flight[53]. We computed the head-direction azimuth (φ) and pitch (θ) of freely flying bats, based on the heading-direction, using the following equations:

$$\varphi = \text{angle}\ (\Delta x + \Delta y \cdot i)$$

$$\theta = \text{angle}\ (\sqrt{\Delta x^2 + \Delta y^2} + \Delta z \cdot i)$$

Where x, y, z are the position of the bat's head in 3D space; Δx, Δy, Δz are the changes in head-position between consecutive video frames; and i is the imaginary number. The 3D head-position (x, y, z) was recorded at 25-Hz using two synchronized video-cameras placed at two of the upper corners of the flight-room (Fig. 5a), which tracked the position of LEDs connected to the wireless head-stage on the bat's head, enabling 3D reconstruction of the animal's 3D head position (see ref. 36). The 3D head position was mildly smoothed using a cubic smoothing spline; Δx, Δy, Δz were computed from these smoothed values.

Spike sorting and criteria for cell inclusion. All spike-sorting procedures were identical to those described previously[9,16,54]. Briefly, spike waveforms were sorted on the basis of their relative energies and amplitudes on different channels of each tetrode (software: SpikeSort3D, Neuralynx; see example in Extended Data Fig. 1). Data from all sessions, including the two sleep sessions, were spike-sorted together. Well-isolated clusters of spikes were manually encircled ('cluster-cutting'), and a refractory period (< 2 ms) in the interspike-interval histogram was verified. In the upright-crawling experiments (setup number 1, Figs 1–3), a total of 266 well-isolated neurons were recorded from dorsal presubiculum of 4 bats. Of these 266 neurons, we included for analysis a total of 122 cells, based on the following criteria: (i) the cell fired at least 30 spikes in each of the upright behavioural sessions; (ii) the cell

was directionally stable between the two upright sessions, with the Pearson correlation coefficient between the one-dimensional (1D) neural tuning curves for azimuth, pitch, or roll being higher than 0.5 ($r \geq 0.5$).

In the ring-experiments (setup number 2, Fig. 4), a total of 180 well-isolated neurons were recorded from the dorsal presubiculum of 2 bats. Of these neurons, we included for analysis 175 cells, based on the following criteria. (i) For computing the tuning curves for pitch, we included only cells that fired at least 25 spikes on the ring during ring-crawling epochs. (ii) For computing the tuning curves for azimuth, we included only cells that fired at least 25 spikes on the floor during floor-crawling epochs. (iii) For comparing pitch tuning on the ring with that on the floor (Fig. 4b, d), and for computing the 2D tuning curves for pitch $\times$ azimuth (Fig. 4h–k), we included only cells that fired at least 25 spikes on the ring and at least 25 spikes during floor-crawling.

In the flight experiments (setup number 3, Fig. 5), a total of 72 well-isolated neurons were recorded from the dorsal presubiculum of one bat. We included for analysis a total of 67 cells, which fired at least 30 spikes during the flight epochs.

Head-direction tuning curves. The head-direction tuning of a neuron was computed as follows: for azimuth tuning, we binned the data in 18 bins of 20 ° each, and computed the firing rate in each bin by dividing the number of spikes in that bin by the time the animal spent in that bin; to compute the neuronal tuning to pitch and roll in the upright-crawling experiments (Figs 1–3), we binned the data in 10 bins of 10 ° each, with each bin labelled according to its centre angle; the extreme bins (labelled as '–45°' and '+45°') contained angles smaller than –40 ° or larger than +40 °, respectively. The resulting 1D tuning curve was smoothed using a rectangular window of size 3 (the smoothing was done on the firing-rate curve, that is, after dividing the unsmoothed spike-curve by the unsmoothed time-spent curve). For azimuth data, the smoothing was applied in a circular manner. Unvisited bins (where total time-spent, before smoothing, was < 2 s) were discarded from analysis. The peak firing rate was defined as the highest rate in the head-direction tuning curve. Tuning width was defined as the width of the tuning curve at 25% of the maximum height ('full tuning width'), where the height was measured from the peak firing rate to the minimal firing rate.

The directionality of the tuning curve in azimuth in the upright-crawling experiments was quantified by computing the Rayleigh vector length of the circular distribution, using the following definition[55]:

$$\text{Rayleigh vector length} = \frac{\pi}{n \cdot \sin\left(\frac{\pi}{n}\right)} \sum_{j=1}^{n} r_{\varphi_j} e^{-i\varphi_j} / \sum_{j=1}^{n} r_{\varphi_j}$$

Where n is the number of circular head-direction bins, φ_j is the direction in radians of the j-th circular bin (namely, $2\pi j/n$), and r_{φ_j} is the average firing rate given the animal's head direction.

In the upright-crawling experiment (setup number 1) we applied a shuffling-based significance test[15,16,25,26], in order to identify neurons that were significantly tuned to azimuth, pitch, or roll. To determine significance in azimuth, we performed the shuffling analysis on the Rayleigh vector length. As pitch and roll were limited in their range and therefore non-circular, we could not use the Rayleigh vector length; instead, to determine significance for pitch and roll, we applied shuffling analysis for the tuning width. Significance was determined for each neuron separately; specifically, for each recorded neuron, the entire sequence of spikes was time shifted by a random (uniformly distributed) time interval, with the end of the session wrapped to the beginning. This preserved the spike number and the temporal structure of the neuron's firing pattern, but dissociated the time of spiking from the animal's actual behaviour. This procedure was repeated 2,000 times for each neuron. A session was defined as tuned to azimuth if its Rayleigh vector length exceeded the 95th percentile of the shuffled distribution for this session. Similarly, a session was defined as tuned to pitch or roll, if the actual tuning width for pitch or roll was narrower than the 95th percentile of the shuffled distribution for this session.

To determine whether a neuron was tuned conjunctively to more than one Euler angle, we first computed the tuning significance of each session for each of the Euler angles independently, based on the shuffling test for the relevant head-direction angle; then, we defined significant 'conjunctive' or 'pure 1D' tuning by taking into account the two upright behavioural sessions, and computing their average 'surprise' function:

$$\text{Average surprise} = -[\log(P_{\text{session 1}}) + \log(P_{\text{session 2}})]/2$$

where P_{session1} and P_{session2} are the P values obtained from the shuffling-based significance tests for upright sessions 1 and 2. A neuron was categorized as directional in azimuth, if its average surprise function in azimuth was ≥ 1.301 (corresponding to significance at $\alpha = 0.05$); similar definition was used to categorize neurons as directional in pitch or roll. If the neuron was significantly directional in more than one head-direction angle, for example, in both azimuth and pitch, it was categorized as a 'conjunctive azimuth $\times$ pitch' cell (for example, Fig. 2d, e). If the neuron was directional only in one head-direction angle, for example, only in azimuth, it was categorized as a 'pure azimuth' cell (for example, Fig. 2b).

Directional tuning in the inverted session was assessed, as in the upright case, using shuffling analysis of the Rayleigh vector length (see Extended Data Fig. 5a). We also analysed the non-significant cells by dividing two non-overlapping groups, those that were 'weakly tuned' under inversion (that is, non-significant, but still clearly tuned) versus truly 'untuned cells' (see Extended Fig. 5d, e). These two groups were separated according to the goodness of fit (R^2) to circular normal function (von Mises function, see below), higher versus lower than $R^2 = 0.45$.

In the ring experiment (setup number 2), azimuth-significant and pitch-significant cells were defined based on shuffling analysis of the respective Rayleigh vector length. Azimuth cells were defined as neurons with significant Rayleigh vector length based on the tuning curve they had on the arena floor (Fig. 4a, pose 1). Pitch cells were defined as neurons with significant Rayleigh vector based on their tuning curve on the ring (Fig. 4a, pose 2). In both cases, Rayleigh vector length and shuffling analysis were similar to those conducted for azimuth cells in the upright-crawling experiment number 1 (see above). In addition, in order to increase the sample size in the ring experiment, we included cells that did not pass the shuffling threshold but had Rayleigh vector length > 0.5. The tuning width of pitch cells in the vertical ring experiment was defined, similarly to azimuth cells, as the width of the tuning curve at 25% of the maximum height, after subtracting the baseline (the minimal firing rate). The analysis of azimuth tuning on the ring (Extended Data Fig. 6) was restricted to azimuth cells whose preferred direction on the arena floor (Extended Data Fig. 6a, b, pose 1) was aligned to the cardinal axis of the ring (east–west, deviating from this axis $<$ half of the mean tuning width). The movement of the inverted bat could be either in the preferred azimuth of the cell (Extended Data Fig. 6a), or in the exact opposite (180°) direction (Extended Data Fig. 6b).

Significant azimuth and pitch cells in flight (setup number 3) were defined in a similar way to their definition in the upright-crawling experiment number 1, based on shuffling analysis of the Rayleigh vector length for azimuth cells, and based on shuffling analysis of the tuning width for pitch cells.

In Fig. 4e–h, we fitted the 1D head-direction tuning curves of neurons with a 1D circular normal function, known also as von Mises function, which has the following form:

$$R_i(\varphi) = c_1 e^{\kappa \cos(\varphi - \varphi_i)} + c_2$$

Where φ is the preferred direction of this unit in radians, φ_i is the direction in radians of the i-th circular bin, and κ, c_1, and c_2 are constants. The quality of the von Mises curve-fitting to the experimental data was used also to assess the unimodality of the neuronal 1D tuning curves (Fig. 4f).

In Fig. 4i, we fitted the 1D azimuth (φ) and 1D pitch (θ) tuning curves of conjunctive neurons with 1D von Mises functions, and combined these 1D functions to generate a 2D von Mises function (Fig. 4i, left):

$$R_i(\varphi,\theta) = c_1 e^{[\kappa_1 \cos(\varphi - \varphi_i) + \kappa_2 \cos(\theta - \theta_i)]} + c_2$$

2D head-direction firing-rate maps. To analyse the conjunctive directional firing-rate maps of presubiculum neurons, we extended the 1D binning used in the section on 'head-direction tuning curves', to 2D head-direction maps (shown in Fig. 2a–e; Extended Data Fig. 3b–e, top; and Extended Data Figs 7 and 8). To construct these 2D maps, we used 18 bins for azimuth, 10 bins for pitch and 10 bins for roll (thus, an azimuth $\times$ pitch map included 18 $\times$ 10 bins, while a pitch $\times$ roll map included 10 $\times$ 10 bins). For each combination of rotation angles, we computed two maps: (i) the time-spent in each 2D directional bin, and (ii) the spike-count per bin. These two maps (time-spent and spike-count) were then individually smoothed using a Gaussian kernel with standard deviation of $\sigma = 1.7$ bins; circular (wrapped) smoothing was applied only for the azimuth in the azimuth $\times$ pitch maps and azimuth $\times$ roll maps. The 2D head direction firing-rate map was then computed for each neuron by dividing bin-by-bin the two smoothed maps of spike count and time spent. Unvisited bins (where total time-spent, before smoothing, was < 0.5 s) were discarded from analysis, unless they were adjacent to a visited bin (with a total time-spent ≥ 0.5 s), and are shown as white bins on the 2D plots. Exclusion based on minimal time spent was different in 1D versus 2D firing maps (2 s versus 0.5 s), because the average time spent in each bin was lower for 2D maps, due to the increase in the dimensionality of the data. The peak firing rate was defined as the highest observed firing rate in any of the bins of the 2D firing-rate map. The 2D maps were plotted with colours normalized between the minimal and maximal firing rate. It is important to note that these 2D maps were plotted for visualization only, while all the statistical tests used for determining the cell category (for example, pure-azimuth cell,

conjunctive azimuth × pitch cell, etc.) were done strictly on the 1D tuning-curves, as described above.

We also plotted 3D firing-rate maps for all 3 Euler angles conjunctively, in a Cartesian representation (azimuth × pitch × roll), as shown in Fig. 2f. These 3D maps were computed in the same way as described in ref. 36 for the case of 3D place cells.

Spatial firing-rate maps and their quantification. To analyse the 2D positional firing-rate maps of presubiculum neurons (Extended Data Fig. 3b–e, bottom), we divided the recording arena into 3.5 × 3.5 cm square bins, and computed a time-spent map and a spike-count maps for each neuron. These two maps were individually smoothed using a Gaussian kernel with standard deviation of $\sigma = 1.7$ bins. The 2D positional firing-rate map was then computed for each neuron by dividing bin-by-bin the two smoothed maps of spike-count and time-spent. Unvisited bins (where total time-spent, before smoothing, was < 0.5 s) were discarded from the analysis, unless they were adjacent to a visited bin (with a total time-spent ≥ 0.5 s), and are shown as white bins on the 2D plots.

The spatial information, in bits per spike, and the sparsity index, were computed from the smoothed firing-rate map of each cell, as described previously[9,16,56,57]:

$$\text{Spatial information (bits/spike)} = \sum p_i (r_i/\bar{r}) \log_2 (r_i/\bar{r})$$

$$\text{Sparsity} = <r_i>^2 / <r_i^2> = (\sum p_i r_i)^2 / \sum p_i r_i^2$$

where r_i is the firing rate of the cell in the i-th bin of the place-field, p_i is the probability of the animal being in the i-th bin (time spent in i-th bin/total session time), $\bar{r}$ is the overall mean firing rate, and i is running over all the visited bins. The spatial-information index is high for neurons with high spatial selectivity. The sparsity index is bound between 0 and 1, with high values indicating poor spatial selectivity.

Angular velocity tuning curves. The angular velocity tuning of a neuron was computed as the time derivative of each of the head-direction angles:

$$\text{Azimuth velocity} = \frac{d\varphi}{dt}$$

$$\text{Pitch velocity} = \frac{d\theta}{dt}$$

$$\text{Roll velocity} = \frac{d\gamma}{dt}$$

For azimuth, the computed angular velocity of the head was binned into 8 bins, each of $25^\circ\,s^{-1}$ (total range between $\pm 100^\circ\,s^{-1}$); for pitch and roll we binned the velocity data into 8 bins, each of $20^\circ\,s^{-1}$ (total range between $\pm 80^\circ\,s^{-1}$). We then computed the firing rate in each bin by dividing the number of spikes in that bin by the time the animal spent in that bin. The resulting curve was smoothed using a rectangular window of size 3. Unvisited bins (where total time spent, before smoothing, was < 0.5 s) were discarded from analysis.

Toroidal representation and correlations between the directional firing-rate maps in the upright versus inverted positions. The two axes of the torus correspond to:

φ (azimuth): the angle of the inter-aural (ear-to-ear) axis projection onto the x–y plane. Notably, this definition of the azimuth in toroidal coordinates results in it being insensitive to rotations in pitch, and thus naturally captures the azimuth direction in both upright and inverted positions.

θ (pitch): the angle of the rostro–caudal axis of the head in the plane which is defined by the z-axis and the projection of the rostro–caudal axis onto the x–y plane. This angle is the common definition of pitch, with the exception that in the toroidal coordinates it is continuous with a cyclical range of $\pm 180^\circ$ (instead of $\pm 90^\circ$).

In order to compare spherical vs toroidal representations, we used the following transformation of Euler angles from spherical to toroidal representation:

$$\text{If position} = \text{upright } \varphi \rightarrow \varphi,\ \theta \rightarrow \theta$$

$$\text{If position} = \text{inverted } \varphi \rightarrow \varphi + 180^\circ,\ \theta \rightarrow 180^\circ - \theta$$

And from toroidal to spherical representation:

$$\text{If } -90^\circ < \theta < 90^\circ\ \varphi \rightarrow \varphi,\ \theta \rightarrow \theta,\ \text{position} = \text{upright}$$

$$\text{If } 90^\circ < \theta < 270^\circ\ \varphi \rightarrow \varphi + 180^\circ,\ \theta \rightarrow 180^\circ - \theta,\ \text{position} = \text{inverted}$$

Specifically, in order to compare spherical versus toroidal representations, we first computed the 2D azimuth × pitch directional rate-maps for the upright and inverted sessions in spherical coordinates, as described above. Then we transformed them into toroidal coordinates, where the outer surface of the torus represents the 2D map for the upright session, while the inner surface represents the 2D map for the inverted session after it underwent two transformations: a shift of all bins along the azimuth dimension by 180°; and flipping the pitch axis. The rationale behind these two transformations is based on two key features underlying the toroidal model:

(i) The first feature is that the azimuth direction of the head in the inverted bat is an extension of the azimuth direction in the upright position (after a shift of 180°), and therefore the upright and inverted positions are not two distinct states but rather a continuum. Therefore, pitching the head at angles greater than +90° will result in flipping the bat from upright to inverted position, and further rotation along the pitch axis will eventually flip the bat back to the upright position, without changing the toroidal azimuth (in contrast, in the spherical model, such a change in pitch will change the azimuth by 180°: compare Fig. 3d to 3c; azimuth values are in blue). For example, the response of a cell to the east direction when the animal is in upright position is given on the outer part of the torus, while the inner side represents the response of the cell to the west direction when the animal is inverted (Extended Data Fig. 7c and right panel of 7d). Therefore, the first step required to transform from spherical to toroidal representation, is shifting all the bins of the 2D directional map of the inverted session (which is computed initially in spherical coordinates) by 180° in azimuth, in order to re-align each azimuth-direction of the inverted session (inner part of the torus) with its equivalent azimuth in the upright session (outer part of the torus).

(ii) The second feature of the toroidal model is that the pitch angle of the head is circular and spans a range of 360° (Fig. 3d), and is computed in the laboratory reference frame (allocentric representation). In order to represent the pitch continuously in the laboratory reference frame, we concatenated the [−90° to +90°] pitch axis of the upright session with the [+90° to −90°] flipped pitch axis of the inverted session, to create a full 360° circular pitch axis. In this way, pitch bins that correspond to adjacent head-pitch in the upright and inverted sessions (adjacent in absolute space, laboratory reference frame) are plotted adjacently to each other on the toroidal manifold.

To test whether the neuronal data are consistent with the toroidal representation, we computed the Pearson correlation coefficient, r, between the 2D directional rate-maps (azimuth × pitch) for each upright session versus the inverted session of the same neuron, under various transformations. We started by comparing the 2D map for the upright session (Extended Data Fig. 7e) with the map for the inverted session before any transformations (Extended Data Fig. 7f), where pitch was represented egocentrically (see Extended Data Fig. 9), relative to the body-reference frame, and the azimuth was not realigned by 180° shift (Extended Data Fig. 7f). Next we compared the 2D map for the upright session versus several angular transformations of the inverted-session map. These transformations of the inverted session included: (i) an azimuth shift of 180° (Extended Data Fig. 7g); (ii) flipping the pitch axis, in order to convert into an allocentric representation (Extended Data Fig. 7h); and (iii) both an azimuth shift of 180° and flipping the pitch (Extended Data Fig. 7i).

Correlation between the upright and the inverted session was computed for the spherical versus the toroidal representation for all cells that were significantly tuned to azimuth or pitch (Fig. 3e). In spherical representation, this correlation was computed between the upright session (for example, Extended Data Fig. 7e) and the inverted session after transformation (ii) above (for example, Extended Data Fig. 7h). In toroidal representation, this correlation was computed between the upright session (Extended Data Fig. 7e) and the inverted session after transformation (iii) above (for example, Extended Data Fig. 7i).

To assess which of these angular transformations is more consistent with the neural data, we computed the increase in correlation (Δ corr, see Extended Data Fig. 7k), defined as the difference in correlation coefficient r before and after applying the indicated angular transformations on the inverted map. For example, to assess how much an azimuth shift of 180° improved the correlation between the upright-session map and inverted-session map, we computed the difference between the correlation r indicated in Extended Data Fig. 7g and the correlation indicated in Extended Data Fig. 7f; and similarly for the other angular transformations. These correlation differences were computed separately for non-overlapping sets of neurons categorized as pure azimuth, pure pitch, or azimuth × pitch cells (see Extended Data Fig. 7k). Analogous calculations were conducted for the head-roll (Extended Data Fig. 7l).

Histology, and functional–anatomical gradients of head-direction cells. Histology was done as described previously[16]. In brief, tetrodes were not moved after the final recording session. The bats were anaesthetized, and in some bats electrolytic lesions (DC positive current of 30 μA, 15-s duration) were done to assist in the precise reconstruction of tetrode positions. Lesions were made every 500 μm

starting from the most ventral recording position. Immediately after doing the lesions, the bat was given an overdose of sodium pentobarbital and, with tetrodes left *in situ*, was perfused transcardially using phosphate buffer saline followed by fixative (4% paraformaldehyde + 0.1 M phosphate buffer saline). The brains were removed and stored in fixative. Subsequently, the right hemisphere was embedded in paraffin, and 10-μM sagittal sections were cut; every third section was mounted on glass slides, resulting in 30-μM intervals between adjacent mounted slides. The sections were then Nissl-stained and coverslip added, and a light microscope fitted with a digital camera was used to determine tetrode placement in the dorsal presubiculum.

The anatomical localization of the recorded head-direction cells was determined by the positions of the tetrodes based on the Nissl sections, together with the documentation of their recording depths. The position along the anterior-posterior axis was measured by projecting the tetrode-track onto a curved line going through the middle of the dorsal–ventral extent of the dorsal presubiculum (an example is shown in Fig. 2h, yellow line). The medio–lateral position of the tetrode track was determined by comparing the recording location to a set of reference sagittal sections with known medio–lateral coordinates (courtesy of M. P. Witter).

For the 1D functional map plots (Extended Data Fig. 4b–e), the percentage of each cell category (pure azimuth, pure pitch, pure roll, or all conjunctive cells) on each tetrode track was calculated out of the total number of directionally significant cells on that tetrode-track. In Extended Data Fig. 4b–e, only tetrode-tracks with $n > 5$ significant cells per track were included in this analysis.

For the 2D functional map plots (Extended Data Figs 4f–h, j, k, m, n), we calculated the percentages based on all the $n = 78$ significant head-direction cells (and not per-tetrode-track as done in Extended Data Fig. 4b–e). Spatial bins of 0.2 × 0.2-mm were used, and an adaptive-binning procedure was applied to increase the bin-size in areas where recordings were sparser. Bins that were further than 500 μm from any significantly-tuned cell in Extended Data Fig. 4f were whitened in Extended Data Fig. 4g, h, j, k, m, n, and were excluded from the analysis. In Extended Data Fig. 4f we plotted all the 266 cells recorded in setup number 1, for display purposes; note that only the significant head-direction cells, indicated by coloured dots, went into computing the 2D maps in Extended Data Fig. 4g, h, j, k, m, n. In Fig. 2i, all the $n = 78$ significant head-direction cells were included, because that analysis was not done per tetrode-track (unlike Extended Data Fig. 4b–e).

Algorithm for reconstructing the 3D head direction (three Euler angles of the head) using one overhead camera. In order to reconstruct the 3D head direction of the bat from 2D tracking data of a single camera, we added a custom 3D tetrahedral arrangement of four LEDs to the recording head-stage on the bat's head (illustrated in Extended Data Figs 11 and 12a). The positions of these LEDs were recorded using a single camera that was placed vertically overhead the arena, and was connected to a video-tracker (Neuralynx) with sampling rate of 25 Hz, which was synchronized to the neural recordings. Combined with the data analysis algorithm described below, this LED arrangement enabled a precise mapping from the position of these four LEDs in the camera image, onto a complete set of coordinates describing the five degrees of freedom of the bat's head. These degrees of freedom include the two spatial coordinates (x, y) for the position inside the arena, and three Euler angles describing the head rotation: yaw ('azimuth', φ), pitch (θ), and roll (γ). Note that in principle there is a degeneracy through which it is impossible to tell whether a bat is upside down; in practice, the context of the experiment resolved this ambiguity, as in our main experiments (see main Figs 1–3) we conducted separate recording sessions for bats crawling upright or being inverted upside-down. To track the inverted position, we placed a mirror on the arena box and tracked the reflections of the LED-array in the mirror, using the overhead camera. Because the LEDs were positioned on a Microdrive on the posterior–dorsal part of the head, opposite from the bat's eyes, the bat could not see the reflections of the LEDs in the mirror. The usage of a mirror allowed us to employ the exact same reconstruction algorithm for 3D head direction as we used in the upright condition; the only change that we did to the algorithm was to adjust it carefully in order to correct for the mirror-symmetry flip of the LEDs' reflections (as seen by the camera) during the inverted session. This adjustment was verified in a calibration session in which we compared upright angles to angles of an inverted headstage that was tracked through the mirror. As in the upright tracking, the head-direction angles in the inverted position were calculated relative to the laboratory reference frame.

For the ring experiments (main Fig. 4) we measured the 3 Euler angles using the overhead camera, as described below, when the bat was crawling on the arena floor (Fig. 4a, pose 1); in contrast, when the bat locomoted on the ring itself (Fig. 4a, pose 2), we measured only the pitch angle of the head using the side camera, and did not measure the other Euler angles (see above for more details about video-tracking in the ring experiments).

Notably, the Euler angles need to be measured with respect to the arena. For example, φ is the angle between the projection of the main axis onto the (x, y) plane (that is, onto the floor of the arena) and between the x axis of the arena coordinate system, as shown in Extended Data Fig. 12a, and it corresponds to the azimuth (yaw) of the head. Similarly, θ is the angle between the main axis and the (x, y) plane of the arena, as illustrated in Extended Data Fig. 12b; θ corresponds to the bat elevating its head upwards or downwards (pitch angle of the head). γ measures the rotation of the device around the main axis, and corresponds to a sideways roll (tilt of the head), as illustrated in Extended Data Fig. 12a. The algorithm extracts these Euler angles from the 2D tracking data in four steps:

1) Derivation of the Euler angles with respect to the plane of the camera (φ_c, θ_c, γ_c) from the image of the 2D projections of the LEDs in the camera coordinate frame (x_c, y_c); see Extended Data Fig. 12a–c.

2) Reconstruction of the 3D position of the four LEDs in the camera coordinate frame (x_c, y_c, z_c), based on the Euler angles (φ_c, θ_c, γ_c) calculated in step 1.

3) Transformation of the 3D positions of the LEDs from the camera coordinates into arena coordinates (x_A, y_A, z_A); see Extended Data Fig. 12d.

4) Derivation of the Euler angles with respect to the arena (φ_A, θ_A, γ_A), computed from the projection of the positions of the 3D LEDs in the arena coordinates onto the arena x–y plane.

φ_A, θ_A, and γ_A are the Euler angles in the arena coordinates, which we computed here; these are the head-direction angles (φ, azimuth; θ, pitch; γ, roll) reported in this study. Note that these angles are given in the absolute room coordinates (allocentric reference frame). The detailed calculations of each step are described below.

To validate this algorithm, we mounted the LED array onto a surgical stereotax (Kopf), which we can rotate and set the Euler angles to known 'ground truth' values, and took video data at various locations (x, y) in the arena, while varying all the three Euler angles in discrete steps over the physiologically relevant range. The comparison of the actual experimentally set angles (as set in the stereotax) and the read-out from the algorithm showed a reliable reconstruction, with a mean absolute error of 5.6 °.

Following are details of the 4 steps used by the algorithm to extract the 3 Euler angles:

Step 1: one aim of the 3D LED apparatus was to enable estimating the Euler angles in the camera frame based purely on the ratios of measured quantities, as this renders the procedure robust against a change of scale (for example, when the animal moves its head up and down, that is, closer or farther from the camera).

By arranging the four LEDs in two offset perpendicular lines (a tetrahedral arrangement, as depicted in Extended Data Fig. 11 and 12a), the relative intersection point between the two lines in the image becomes a function of θ_c and γ_c, while φ_c can be determined using the projection of the main axis ($\mathbf{P_1}$, $\mathbf{P_2}$) onto the plane of the arena as seen from the camera ('the camera plane'). Based on this, the camera angles can be derived using the following relations: we define the geometry of the LED arrangement as shown in Extended Data Fig. 12a, where f_1 is the distance from the centre of the LED arrangement along the main axis to the front red LED, while f_2 is the distance from the centre to the rear green LED; h is the height between the main top axis and the transverse axis; r_1 and r_2 are the distances from the centre to the right and to the left blue LEDs, respectively; a_1, a_2, b_1, and b_2 are the distances of the projection along the camera plane of the 4 arms of the LED arrangement (that is, front, rear, right, and left, respectively), as defined in Extended Data Fig. 12c (the dashed blue and dashed orange lines in Extended Data Fig. 12c denote the projections onto the camera plane of the LEDs and the segments connecting them, and are plotted also in Extended Data Fig. 12a; the dashed orange line is plotted also in Extended Data Fig. 12b).

α_c is defined as the distance of one of the blue LEDs from the intersection point, in the camera plane, normalized to the distance between the two blue LEDs in the camera plane:

$$\alpha_c = b_1/(b_1 + b_2) = [r_1 \cos(\gamma_c) - h \sin(\gamma_c)]/[(r_1 + r_2) \cos(\gamma_c)] \quad (1)$$

We now define the subscript '0' as the corresponding ratio in the neutral position ($\varphi_c = \theta_c = \gamma_c = 0$), which can be determined from the known geometry of the device. Thus α_0 is the same normalized distance in the limiting case of $\gamma_c = 0$:

$$\alpha_0 = r_1 / (r_1 + r_2) \quad (2)$$

From (1) and (2) it follows that:

$$\alpha_0 - h \tan(\gamma_c) / (r_1 + r_2) = \alpha_c \quad (3)$$

From (3) we can derive γ_c:

$$\gamma_c = \text{atan}\,[(\alpha_0 - \alpha_c)\,(r_1 + r_2) / h\,] \quad (4)$$

Similarly, β_c is defined as the distance of the red LED from the intersection point in the camera plane, normalized to the distance between the red and green LEDs in the camera plane:

$$\beta_c = a_1/(a_1+a_2) = [f_1\cos(\theta_c) - h'\sin(\theta_c)]/[(f_1+f_2)\cos(\theta_c)] \quad (5)$$

where:

$$h' = h / \cos(\gamma_c) \quad (6)$$

given:

$$\beta_0 = f_1 / (f_1 + f_2); \quad (7)$$

Where, as before, the subscript '0' defines the corresponding ratio in the neutral position. See Extended Data Fig. 12b for illustration of the angle θ_c.

From (5) and (7) it follows that:

$$\beta_0 - h' \tan(\theta_c) / (f_1 + f_2) = \beta_c \quad (8)$$

Finally, from (6) and (8) we derive θ_c:

$$\theta_c = \text{atan}\ [\ (\beta_0 - \beta_c)\ (f_1 + f_2)\ \cos(\gamma_c) / h\ ] \quad (9)$$

To derive φ_c:

$$\mathbf{v} = \mathbf{P_1} - \mathbf{P_2} \quad (10)$$

Where $\mathbf{P_1}$ and $\mathbf{P_2}$ are the projections of the red and green LEDs on the camera plane, respectively (see Extended Data Fig. 12a).

It follows that:

$$\varphi_c = \text{atan}[\ v_y / v_x\ ] + \pi\ H(-v_x) \quad (11)$$

Where v_x and v_y are the x and y components of the vector **v**, H() is the Heaviside step-function, and atan[x] is assumed to be the principal branch of tan, with atan[x] between $-\pi/2$ and $\pi/2$.

Taken together, the Euler angles derived here (φ_c, θ_c, γ_c) are computed in the camera frame, based on the position of the LEDs in the camera plane.

Step 2: having obtained the Euler angles in the camera frame in step 1, the 3D position of the four LEDs can now be calculated in camera coordinates by applying a rotation matrix with the obtained Euler angles, in order to rotate the device from the neutral 'zero' orientation (that is, non-tilted, upright position) to the view in the camera frame:

$$(x_c, y_c, z_c) = \text{ROT}(\varphi_c, \theta_c, \gamma_c)\ (x_0, y_0, z_0) \quad (12)$$

where (x_0, y_0, z_0) is the configuration of the four LEDs in the neutral orientation, (x_c, y_c, z_c) is the configuration of the four LEDs in the camera frame, and ROT(φ_c, θ_c, γ_c) is the standard rotation matrix defined by the Euler angles derived in step 1.

Step 3: when the bat is in the centre of the arena, straight under the camera (position (0,0)), the camera and arena frames are perfectly aligned. However, in general the device is off-centre, and the difference between the two frames needs to be accounted for. An example of this mis-alignment of the two coordinate frames is shown in Extended Data Fig. 12d. In order to obtain the position of the LEDs in arena coordinates (x_A, y_A, z_A), the basis vectors of the camera frame $\mathbf{X_C}$, $\mathbf{Y_C}$ and $\mathbf{Z_C}$ need to be expressed in arena coordinates, that is: $\mathbf{X_A}$, $\mathbf{Y_A}$ and $\mathbf{Z_A}$ (Extended Data Fig. 12d). By construction, $\mathbf{Z_C}$ is in line with the line-of-sight from the centre of the device to the camera. The camera plane is perpendicular to $\mathbf{Z_C}$ and is spanned by $\mathbf{X_C}$ and $\mathbf{Y_C}$, where $\mathbf{X_C}$ is the normalized projection of $\mathbf{X_A}$ onto the camera-plane. From requiring $\mathbf{Y_C}$ to be perpendicular to both $\mathbf{X_C}$ and $\mathbf{Z_C}$, it follows that:

$$\mathbf{Y_C} = \mathbf{X_C} <\text{cross}> \mathbf{Z_C} \quad (13)$$

Having obtained the local coordinate transformation connecting arena and camera coordinates, this transform can be applied to the 3D coordinates of the LEDs obtained in step 2, in order to determine their position in the arena frame:

$$(x_A, y_A, z_A) = T^{-1}{}_{A\to C}\ (x_c, y_c, z_c) \quad (14)$$

Where $T_{A\to C}$ is the transformation matrix defined by the basis vectors $\mathbf{X_C}$, $\mathbf{Y_C}$ and $\mathbf{Z_C}$. Note, that the transformations $T_{A\to C}$ and $T^{-1}{}_{A\to C}$ include both translation and rotation of the coordinate frame.

Step 4: in step 1 we used the fact that all three Euler angles with respect to a given coordinate frame can be determined from just the *x*–*y* projection of the LED-coordinates. Hence, it is sufficient to consider the *x*–*y* values of the reconstructed device in the arena frame, and then to re-apply the relations used in step 1, in order to obtain the final angles with respect to the arena. Namely from equations (4), (9) and (11) we can derive the Euler angles in arena coordinates:

$$\gamma_A = \arctan\ [\ (\alpha_0 - \alpha_A)\ (r_1 + r_2) / h\ ] \quad (15)$$

$$\theta_A = \arctan\ [\ (\beta_0 - \beta_A)\ (f_1 + f_2)\ \cos(\gamma_A) / h\ ] \quad (16)$$

$$\varphi_A = \text{atan}[\ v_y / v_x\ ] + \pi\ H(-v_x) \quad (17)$$

Where v is defined similarly to equation (10), but for the projection onto the arena plane.

The Euler angles (φ_A, θ_A, γ_A) in the arena coordinates, which we computed here (equations 15–17), were the head-direction angles (φ, azimuth; θ, pitch; γ, roll) that were reported in this study.

51. Neuweiler, G. *The Biology of Bats* (Oxford Univ. Press, 2000).
52. Altringham, J. D. *Bats: Biology and Behaviour* (Oxford Univ. Press, 1996).
53. Yovel, Y., Geva-Sagiv, M. & Ulanovsky, N. Click-based echolocation in bats: not so primitive after all. *J. Comp. Physiol. A* **197,** 515–530 (2011).
54. Ulanovsky, N. & Moss, C. F. Dynamics of hippocampal spatial representation in echolocating bats. *Hippocampus* **21,** 150–161 (2011).
55. Zar, J. H. *Biostatistical Analysis* 4th edn (Prentice Hall, 1998).
56. Skaggs, W. E., McNaughton, B. L., Gothard, K. M. & Markus, E. J. An Information-theoretic approach to deciphering the hippocampal code. *Advances in Neural Information Processing Systems* **5,** 1030–1037 (1993).
57. Skaggs, W. E., McNaughton, B. L., Wilson, M. A. & Barnes, C. A. Theta phase precession in hippocampal neuronal populations and the compression of temporal sequences. *Hippocampus* **6,** 149–172 (1996).
58. Cacucci, F., Lever, C., Wills, T. J., Burgess, N. & O'Keefe, J. Theta-modulated place-by-direction cells in the hippocampal formation in the rat. *J. Neurosci.* **24,** 8265–8277 (2004).
59. Sharp, P. E. Multiple spatial/behavioral correlates for cells in the rat postsubiculum: multiple regression analysis and comparison to other hippocampal areas. *Cereb. Cortex* **6,** 238–259 (1996).

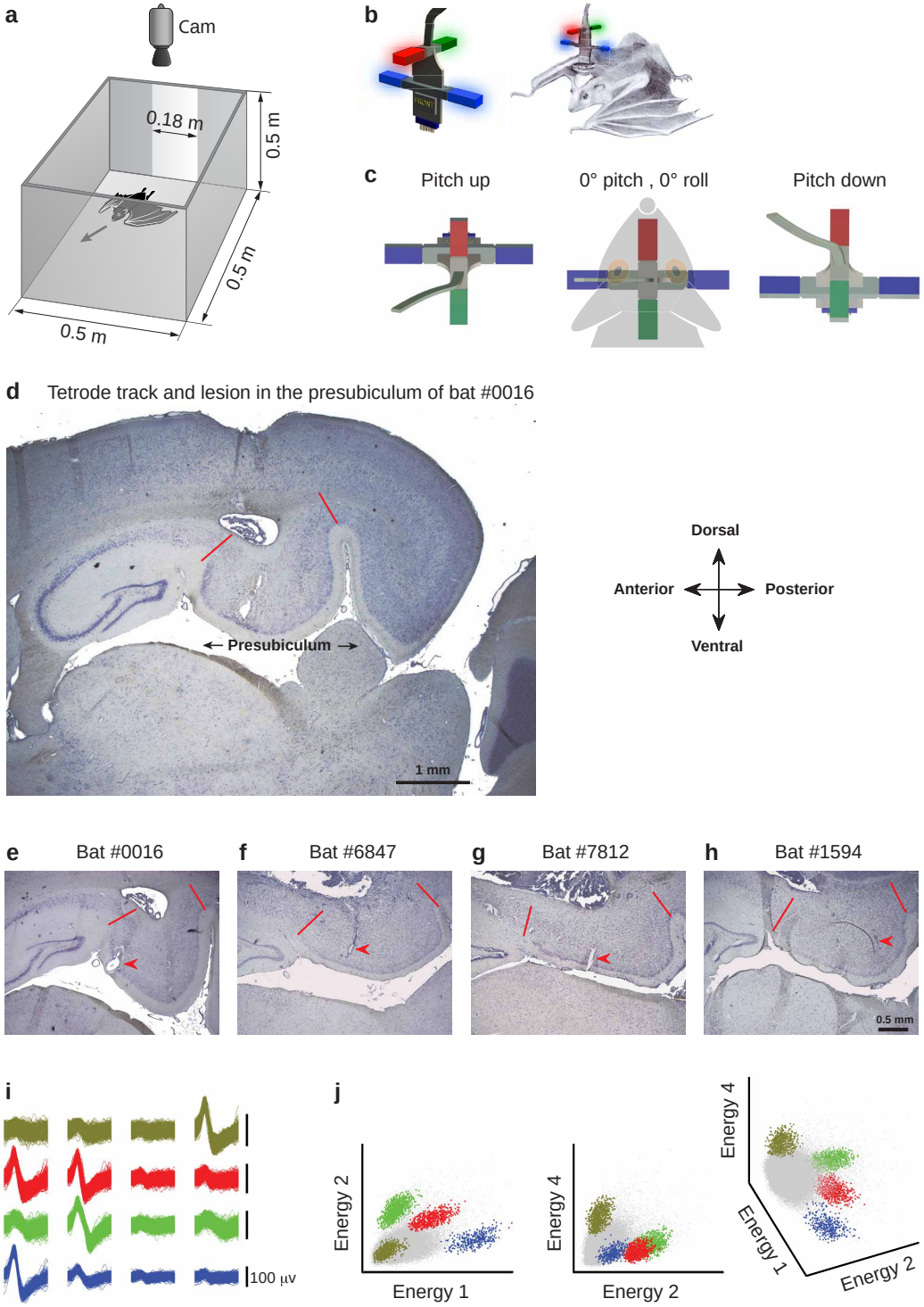

Extended Data Figure 1 | Experimental methods for behavioural setup number 1, recording locations, and example of spike-sorting. **a**, Schematic illustration of the behavioural arena and camera position used in the crawling experiments (setup number 1). **b**, Illustrations of the device used for computing the head-direction Euler angles, which was based on a 3D non-coplanar arrangement of four LEDs. This four-LED device was mounted on the recording headstage, and allowed measuring the Euler angles using one overhead camera (see Methods and Extended Data Figs 11 and 12 for details of the algorithm). **c**, Schematic camera views of the four-LED headstage at different pitch angles. **d**, Nissl-stained sagittal brain section through the hippocampal formation of an Egyptian fruit bat, including the dorsal presubiculum (same brain section as in Fig. 1c). Electrolytic lesions were done at the end of the experiment. Red lines denote the borders of the presubiculum. Scale bar, 1 mm. **e**–**h**, Sagittal Nissl-stained brain sections showing representative recording sites in the presubiculum of 4 bats. Tetrode tracks are marked by red arrowheads (the arrowheads point to lesion sites in bats number 0016 and 6847; while in bats number 7812 and 1594, the arrowheads point to the end and to the middle of the tetrode-track, respectively). Sections in **d** and **e** are from the same animal (bat 0016); the section in **e** shows the track of a different tetrode than the one seen in **d**. Scale bar in **e**–**h**, 0.5 mm. **i**, Waveforms of four different neurons (different colours, rows) recorded simultaneously on the 4 channels of a single tetrode (columns). Scale bar, 100 µV; waveform duration, 1 ms. **j**, Energy displays (cluster plots) for the data in **i**, showing the energy of spikes (dots) on two of the tetrode's four channels (left and middle panels), or on three of the tetrode's four channels (right panel). Colours match the waveforms in **i**; grey dots, small spikes or noise that crossed the voltage threshold but were not classified as single units.

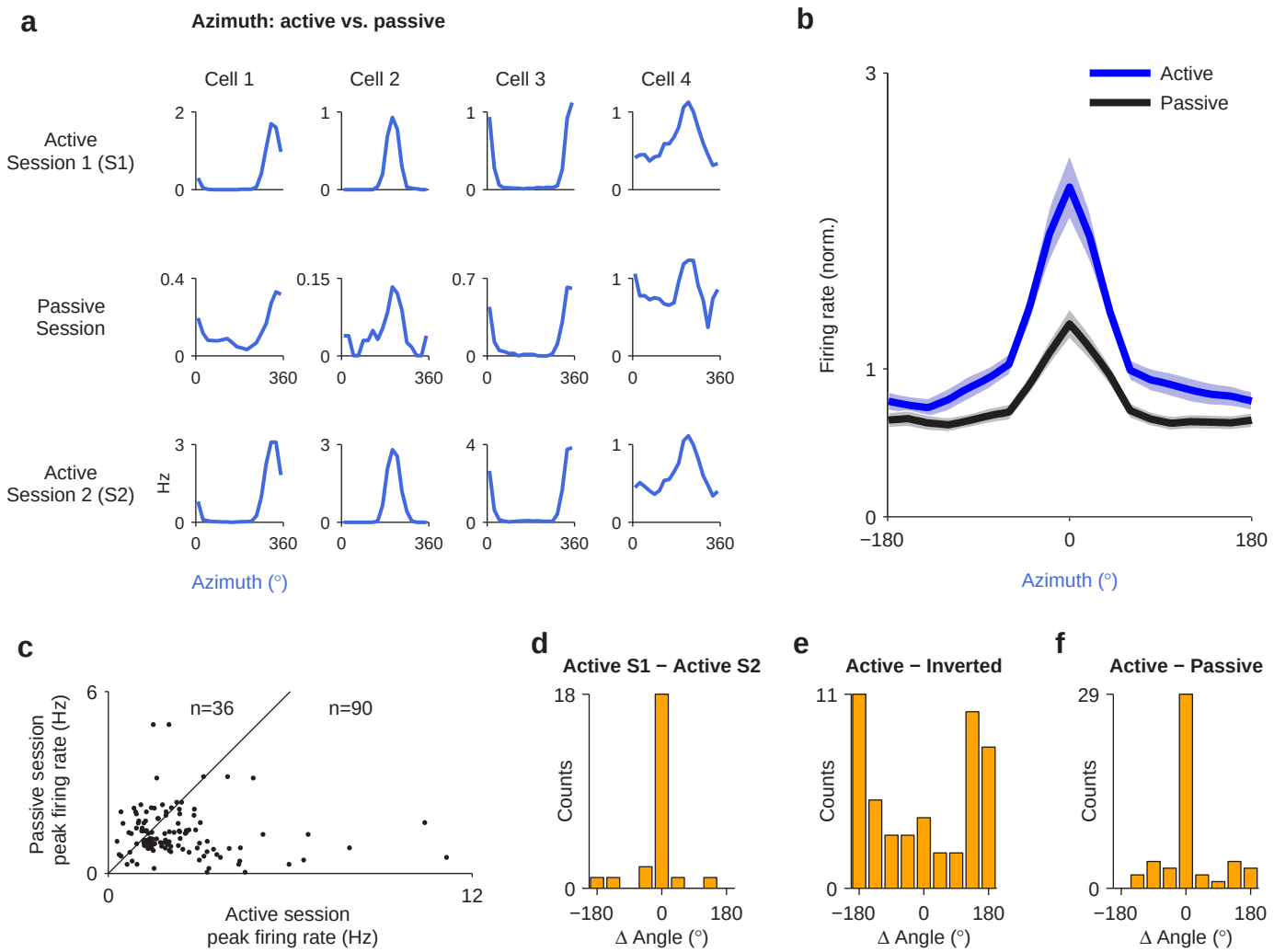

Extended Data Figure 2 | Head-direction cells maintain their preferred azimuthal direction when the bat is being moved passively in the upright position. **a**, Azimuth tuning of four example cells in three upright sessions: active session number 1 (top row), passive session (middle), and active session number 2 (bottom). Note that the preferred direction in the passive session stayed similar to the preferred direction of the active sessions, despite the reduction in cells' firing rate during the passive session. **b**, Population average tuning curve for active (blue) versus passive (black) sessions, for all azimuth-significant cells ($n = 63$ cells); shading, mean ± s.e.m. Prior to averaging, the tuning-curve of each neuron was centred around its peak, and the firing rate was normalized to the mean firing rate of the neuron across all sessions (active and passive pooled together). Note that, on average, presubiculum neurons exhibited a lower firing rate during the passive session as compared to the active sessions. **c**, Peak firing rate of azimuth-tuned neurons ($n = 63$ cells, that is, 126 sessions) in the active versus passive sessions, showing a significantly lower firing rate during the passive condition (sign test, $P < 0.001$; number of sessions above and below the diagonal are indicated on the graph). The peak firing rates of these neurons ranged up to 12 Hz, and were generally lower than peak firing rates in rats, similar to what we found previously for hippocampal place-cells and entorhinal grid-cells in crawling bats[9,16,54], and consistent with the slow crawling velocity of bats, which reduces the firing rate[36,40]. Importantly, even cells with low firing rates exhibited stable directional tuning across sessions (see panel **a**). **d**–**f**, Changes in tuning properties during inversion are not caused by the passivity of the movement in the inverted session. **d**, Distribution of angular differences in the preferred azimuthal head direction between the two active behavioural sessions (S1 and S2). The histogram was plotted for cells with significant tuning in the upright active sessions that also had significant tuning in the inverted session. Peak around 0° indicates stability of the azimuthal tuning across the two active behavioural sessions. **e**, Angular difference between the upright sessions and the inverted session. Peaks at around ± 180° indicate that inversion of the bat upside-down resulted in a 180° shift in the preferred azimuthal direction for the azimuth cells. **f**, Angular difference between the active upright sessions and the passive (upright) session. Peak around 0° indicates that passive movement in itself does not induce a change in the preferred direction of the neurons (see also examples in **a**).

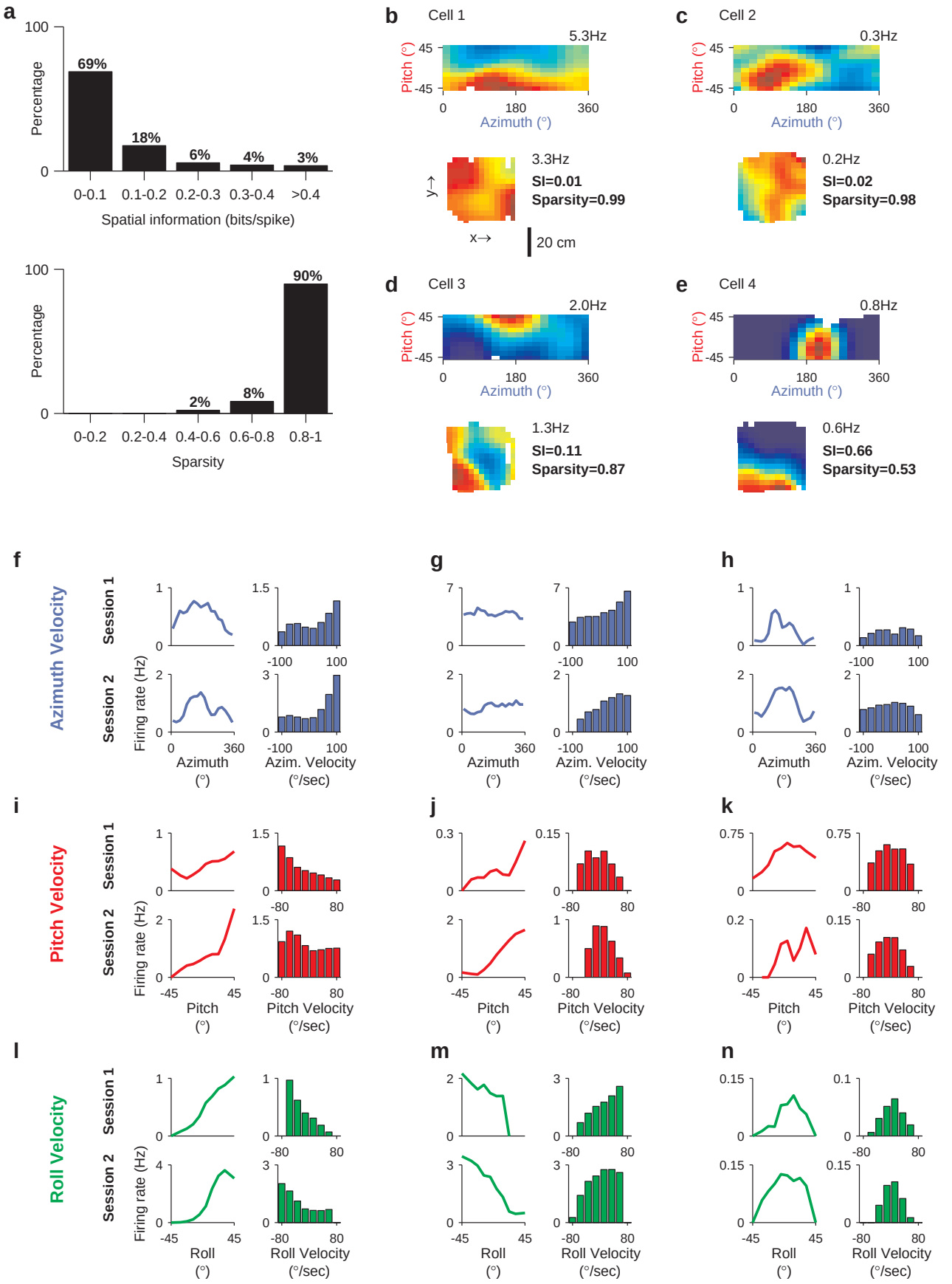

Extended Data Figure 3 | Bat presubiculum neurons are modulated by angular velocity but exhibit weak spatial tuning. **a**, Distribution of spatial information (top) and sparsity (bottom) for all the 122 presubiculum neurons recorded in setup number 1. Note that, with a few exceptions, neurons in the presubiculum conveyed little information about the location of the bat in the environment and displayed weak spatial selectivity, as indicated by their low spatial-information index and high sparsity index. **b**–**e**, Examples of four neurons, depicting the head-direction fields (top) and place-fields (bottom); spatial information (SI) and sparsity for each neuron are indicated next to the positional plot; the cells were ordered according to spatial information values. Most neurons (**b**–**d**) carried little spatial information and showed irregular spatial firing patterns, despite having significant directional responses. Only 3% of the neurons had spatial information >0.4 bits per spike (for example, the cell in **e**), in addition to their directional tuning. This small minority of cells could possibly be border/boundary cells[18–20], or place-by-direction cells[37,58], or perhaps conjunctive grid $\times$ head-direction cells[15,24] (we could not detect grid structure because of the small size of the arena, 50×50 cm). **f**–**n**, Head-direction cell activity is modulated by angular velocity. Shown is the tuning to head direction (left) and angular velocity (right) for 9 examples from 8 neurons (panels **f** and **i** are from the same neuron). Top row (**f**–**h**): azimuth and azimuth-velocity; middle row (**i**–**k**): pitch and pitch-velocity; bottom row (**l**–**n**): roll and roll-velocity. **f**, A neuron tuned to azimuth (left panels) that increases its firing rate in response to faster turning in the clockwise direction (right panels). **g**, A neuron that did not exhibit any tuning to head direction in azimuth (left panels), but nevertheless increased its firing rate with increasing head velocity in the clockwise direction (right panels); this neuron might be classified as a pure 'angular velocity neuron'. **h**, A neuron tuned to azimuth that exhibited almost no modulation by azimuth-velocity; this neuron might be classified as a pure 'head-direction neuron'. **i**, A neuron tuned to pitch, which increased its firing rate in response to fast decrease in pitch. Note that this is in fact a conjunctive azimuth $\times$ pitch neuron (same neuron as in **f**). **j**–**k**, Pitch-tuned neurons that also fired preferentially to slow angular head-velocity in pitch. **l**–**n**, Roll-neurons that were also modulated by anti-clockwise angular-velocity in roll (**l**), clockwise angular-velocity in roll (**m**), or slow-roll velocity (**n**). These diverse types of tuning to angular-velocity resemble the functional diversity of azimuth–velocity tuning reported for presubiculum neurons in the rat[4,59], and also suggest that bat presubiculum neurons can integrate head angular-movements in rotation planes other than Earth's horizontal plane.

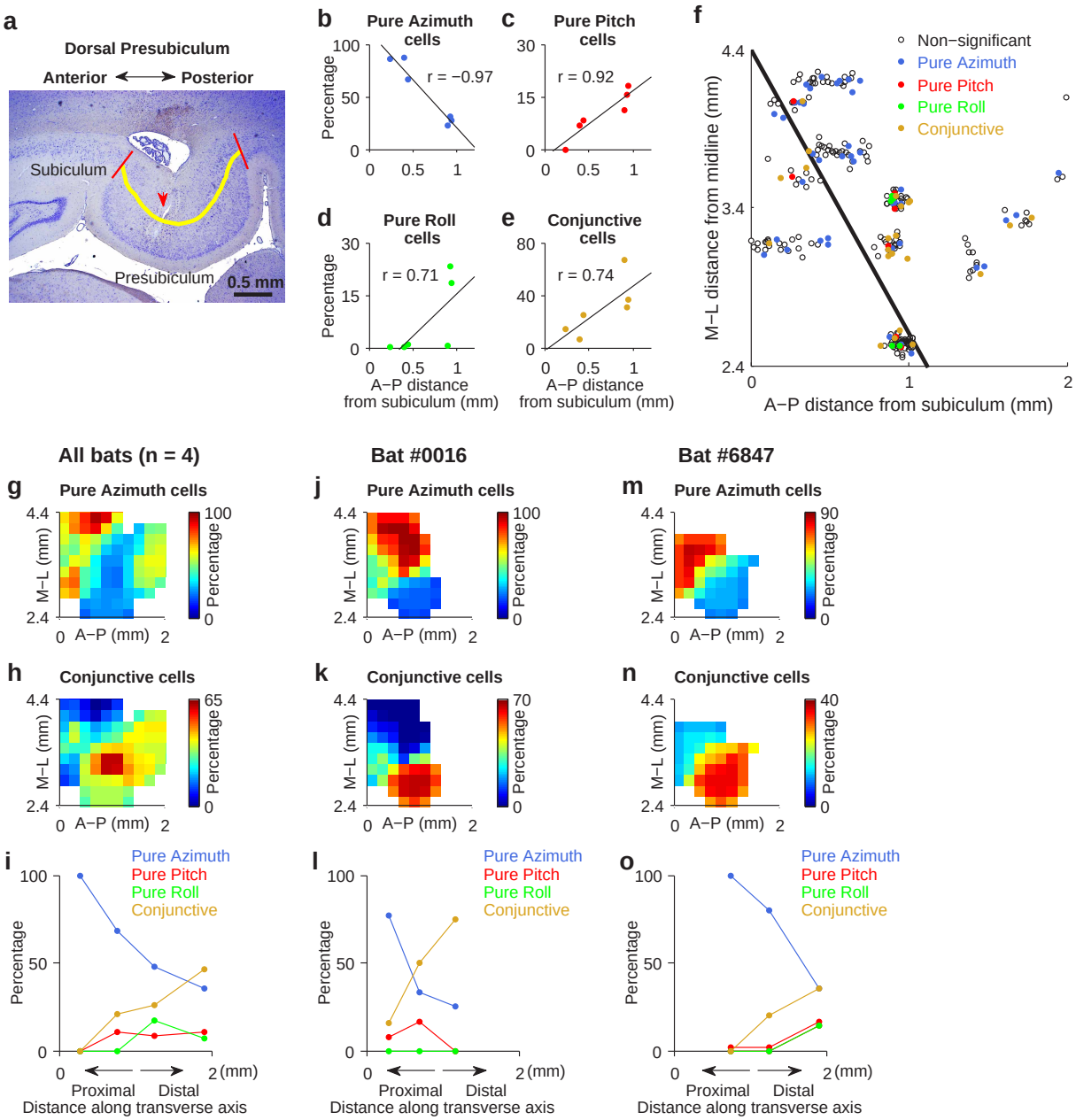

Extended Data Figure 4 | Functional–anatomical gradient of head-direction cells along the transverse axis of dorsal presubiculum. **a**, Sagittal section through the presubiculum; red lines, presubiculum borders. Yellow line shows the axis used to determine the anterior–posterior distance of the tetrode-track (arrowhead) from the subiculum border. Scale bar, 0.5 mm. **b**–**e**, Percentage of head-direction cells in each tetrode-track, plotted against the anterior-posterior ('A–P') distance of that tetrode-track from the subiculum. Each dot represents one tetrode-track; shown are only tetrode-tracks with >5 significant head-direction cells recorded per track. Percentages plotted separately for neurons with pure tuning to azimuth (**b**), pitch (**c**), or roll (**d**), and for neurons with conjunctive tuning to any angular combination (**e**); regression lines are also indicated. **f**, 2D unfolded map of dorsal presubiculum, showing the reconstructed recording location for all the 266 neurons recorded from the 4 bats in setup number 1. Colours indicate pure tuning to azimuth (blue), pitch (red), or roll (green), or neurons with conjunctive tuning to any angular combination (yellow); cells that did not pass the criterion for stability or directionality are also shown (empty circles). Note that the antero-posterior (A–P) distance is measured along the curved structure of the presubiculum (as shown by the yellow line in Fig. 2h), while the medio–lateral (M–L) distance is measured straight from midline. The multilinear regression line (black) was computed from the 2D maps in **g**, **h**. Dots were slightly jittered, for display purposes only, to prevent overlap. **g**, **h**, Two-dimensional unfolded maps of dorsal presubiculum from the 4 bats tested in setup number 1, showing the percentage of pure azimuth (**g**) and conjunctive cells (**h**), based on the recording locations of individual cells (M–L, medio–lateral distance from midline; Methods). These maps reveal a functional gradient along a diagonal axis, with pure azimuth cells dominating the anterolateral part and conjunctive cells the posteromedial part of dorsal presubiculum. From these maps, we calculated the multilinear regression line (black line in **f**), based on A–P and M–L positions as predictors. This line represents the axis of the maximal diagonal gradient of head-direction cells, and is computed as the slope of the multilinear regression coefficients, averaged for pure azimuth and for conjunctive cells, which together represent the majority of the head-direction cells. **i**, Percentages of all 4 neuronal types from **b**–**e**, binned here along the diagonal axis (regression line) of the functional gradient, which corresponds to the transverse axis of the presubiculum (Methods; graph based on all the significant head-direction cells from the 4 bats in setup number 1: $n = 78$ neurons). **j**–**o**, Same as in **g**–**i**, computed now for two individual bats in which at least 3 tetrodes were identified within the dorsal presubiculum, which is the minimum number of tetrode-tracks that allowed us to create a functional–anatomical map for an individual animal (**j**–**l**, bat number 0016, $n = 36$ significant head-direction cells; **m**–**o**, bat number 6847, $n = 21$ significant head-direction cells).

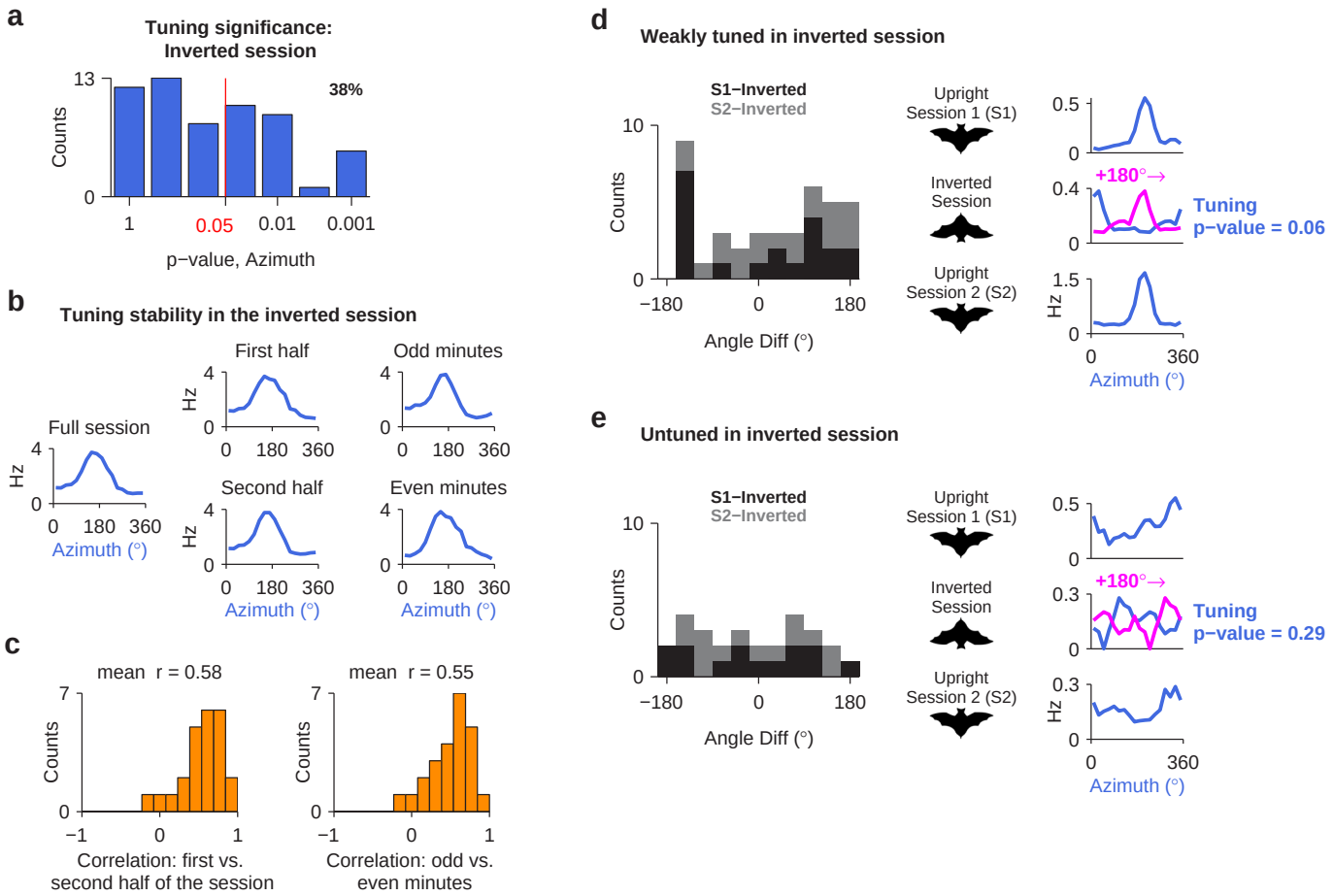

Extended Data Figure 5 | Azimuth tuning and stability analysis for neurons in the inverted session. **a**, Distribution of tuning significance of azimuth-encoding cells ($n = 63$), in the inverted session (setup number 1). Red line, 95th percentile value from shuffled data. **b**, **c**, Stability analysis of azimuth cells in the inverted session. **b**, Example of azimuth tuning for a single cell. Left, tuning curve computed for the entire inverted session. Middle column, comparing the tuning curve computed for the first half versus the second half of the inverted session. Right column, comparing the tuning curve computed for odd versus even minutes of the inverted session. **c**, Distribution of correlation coefficients for azimuth cells with significant tuning in the inverted session ($n = 24$), parsed based on two partitioning conditions. Left, first half versus second half of the session; right, odd versus even minutes. **d**, Left, distributions of differences in preferred direction between sessions, for cells that have not reached tuning-significance criterion (that is, neurons to the left of the red line in **a**), but were nevertheless somewhat tuned in azimuth in the inverted session ('weakly tuned', $n = 20$; see Methods). Distribution of angular differences between each of the upright sessions and the inverted session (S1–inverted, S2–inverted) of these 'weakly tuned' neurons shows peaks near $\pm 180^\circ$ for the inverted session, indicating 180°-shift of the preferred direction, similar to that observed in azimuth cells that were significantly tuned under inversion (Fig. 3b, bottom). Right, azimuth tuning of an example cell that did not pass the shuffling criterion for tuning under inversion, but was close to significance ($P = 0.06$); this neuron was considered 'weakly tuned' by our criteria, but nevertheless this neuron showed a shift of 180° in the inverted session (middle plot, blue) relative to the upright sessions (top and bottom). Magenta curve in the middle row: the tuning-curve of the inverted session, shifted by 180°. **e**, Left, same as in **d**, for the remainder of the cells that have not reached significance criterion and were indeed untuned in the inverted session (that is, these cells were to the left of the red line in panel **a**, and were also very clearly not directionally tuned: 'untuned cells', $n = 11$; Methods). Right, an example cell with very little tuning under inversion (test for tuning significance for this neuron: $P = 0.29$).

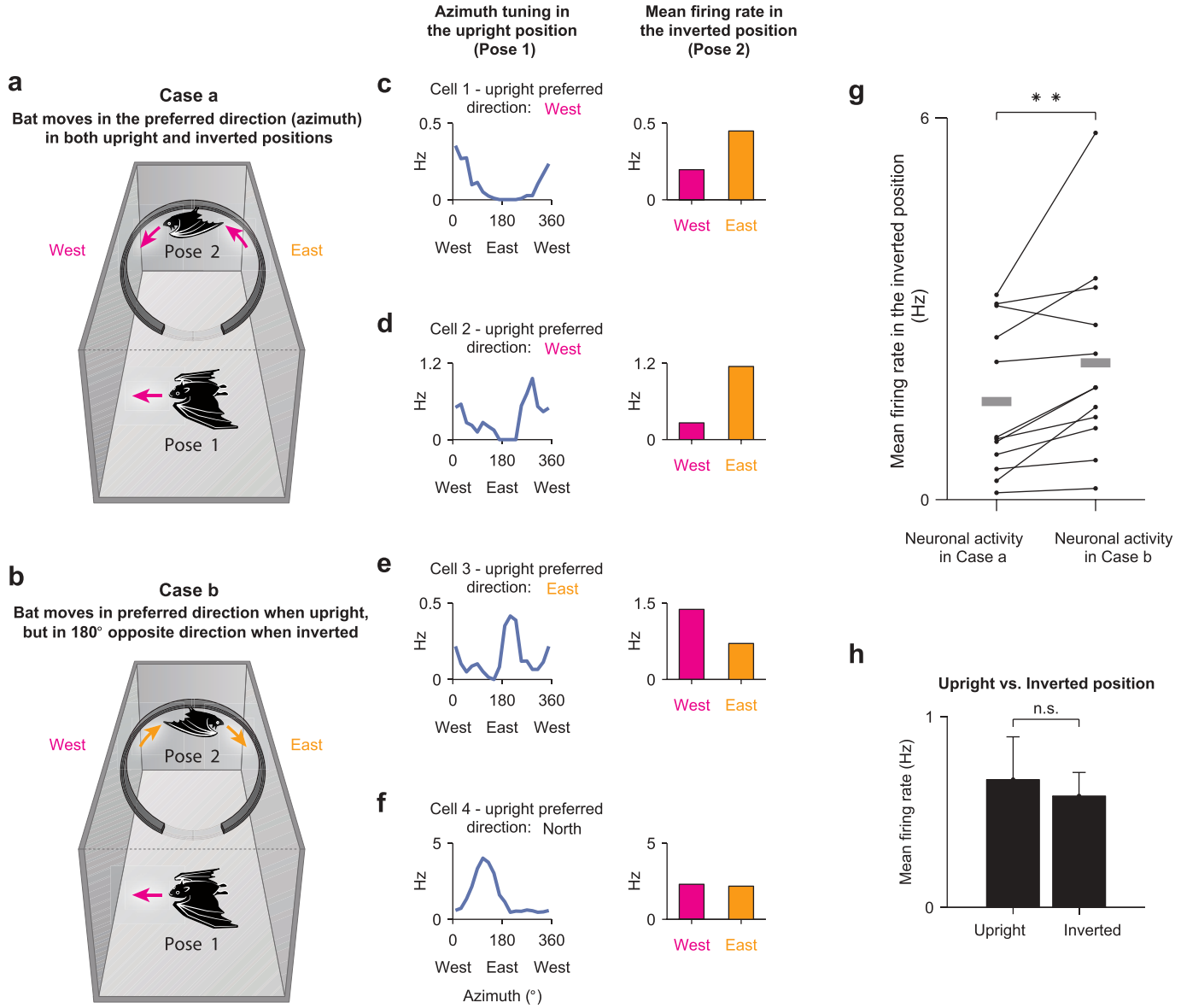

Extended Data Figure 6 | Azimuth cells exhibit a 180°-shift in their preferred direction when bats position themselves upside-down on their own volition. **a**, **b**, Schematic illustration of the vertical-ring apparatus (setup number 2), designed to compare the tuning properties of neurons during upright crawling on the arena floor (pose 1) with the activity of the same neurons during epochs in which the bat had positioned itself upside-down on its own volition along the inner side of a vertical ring (pose 2). The analysis was restricted to azimuth cells whose preferred direction on the arena floor was aligned to the cardinal axis of the ring (west–east), so that movement of the inverted bat would be either in the upright-preferred-direction of the neuron (case a), or in the exact opposite (180°) direction (case b). **c**–**e**, Examples of azimuth cells, showing reversed firing in animals that positioned themselves upside down on their own volition. Left, azimuth tuning curves of individuals neurons during upright locomotion on the arena floor (pose 1). Right, mean firing rates of the same neurons during active inverted motion (pose 2), shown separately for west and east directions. **c**, **d**, Two example cells with west direction tuning on the arena floor (left, blue curves), showing a reversal of their firing direction in the inverted position (right, increase in firing to the east). **e**, Example cell with east direction tuning on the arena floor, showing a reversal of its firing direction in the inverted position (increase in firing to the west). **f**, Example cell, whose preferred direction on the floor was orthogonal to the cardinal axis of the ring (preferred direction was to the north). Note that this neuron showed no preference to either west or east directions in the inverted position (right). **g**, Pairwise comparison of mean firing rates of azimuth cells in the inverted position, for epochs in which the inverted bat moved in the upright-preferred-direction of the neuron (case a, as shown in panel **a**), versus epochs in which it moved in the opposite (180°) direction (case b, as shown in panel **b**). Notably, 92% of the cells ($n = 11/12$) increased their firing rate when the head-azimuth in the inverted position was 180° opposite to the upright-preferred-direction of the cells, as predicted by the torus model. $^{**}P < 0.01$. **h**, Comparison of mean firing rates in the upright position versus the inverted position for the azimuth cells analysed in **g**, showing no significant change in the mean firing rate under inversion. Error bars, mean ± s.e.m.

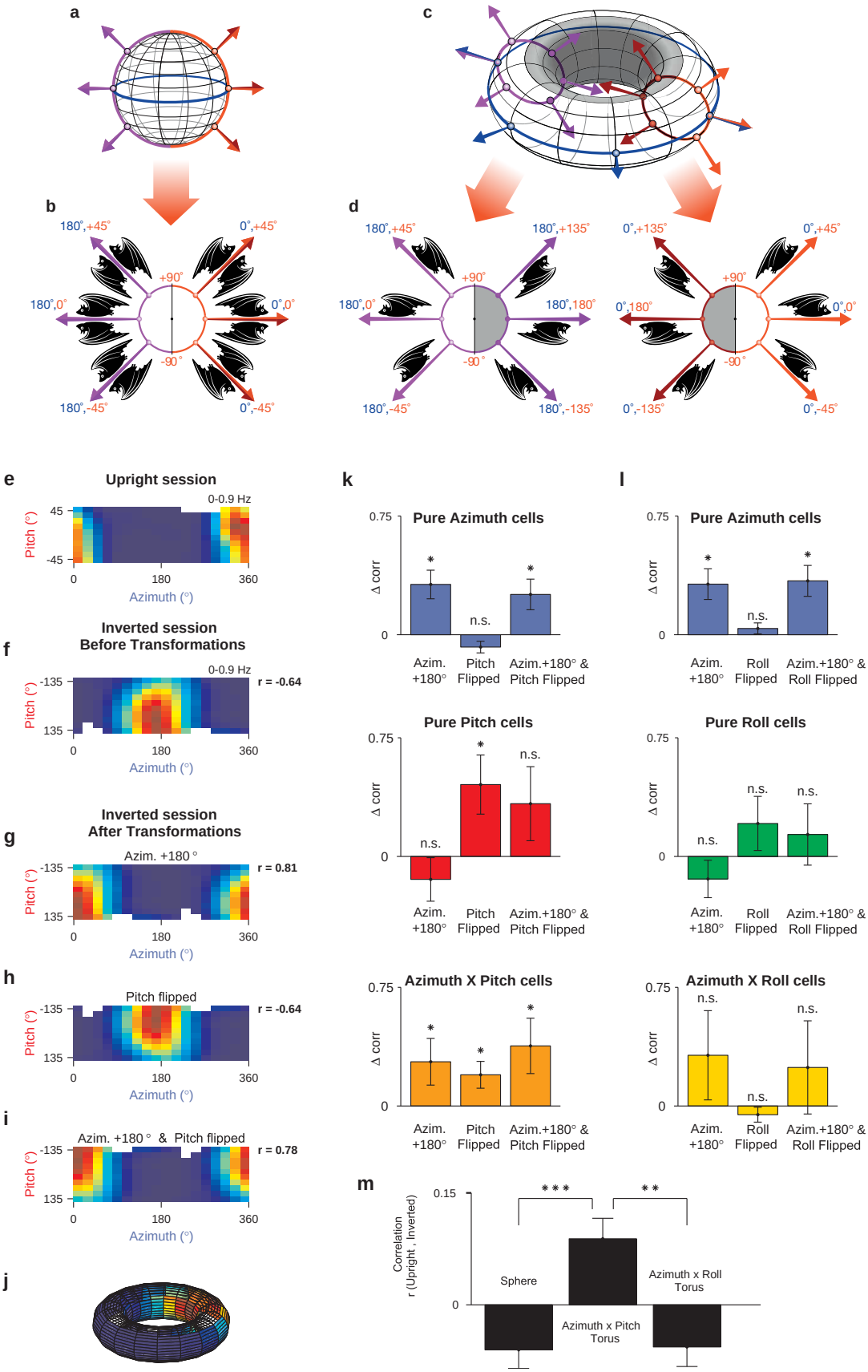

Extended Data Figure 7 | Spherical versus toroidal coordinate systems. **a**, In a spherical coordinate system, which describes the direction of a vector in 3D space, 3D head direction is defined by its azimuth and pitch angles. Each line of longitude on a sphere corresponds to a specific azimuth. The position of the head along this line of longitude is given by its pitch angle (ranging from –90° to +90°). For example, the east longitude (red-coloured half-ring) corresponds to different pitch angles along the 0° azimuth. The west longitude (purple-coloured half-ring) corresponds to different pitch angles along the 180° azimuth. **b**, The azimuth and pitch angles of the head in spherical coordinates define its absolute direction in 3D, regardless of whether the bat is upright or inverted. For example, the spherical coordinates of the bat furthest on the right in this plot (0° azimuth, 0° pitch), correspond to an upright bat with its head parallel to the horizontal plane facing the east direction but also to an inverted bat facing east (also parallel to the ground). Thus, the spherical representation is ambiguous with respect to the upright versus the inverted state. **c**, In the toroidal coordinate system, the two angles that determine the direction of the animal's head in 3D (azimuth and pitch) represent two independent cyclic degrees of freedom, both having a range of 360° (blue circle, azimuth; red and purple circles, pitch). Importantly, the toroidal azimuth does not represent the direction of the animal's nose (rostro–caudal axis) relative to a distal point in space, but rather the direction of the inter-aural axis. The toroidal pitch, in contrast, is anchored to the direction of the rostro–caudal axis. In this representation, any rotation in pitch does not change the azimuth, as defined in toroidal coordinates (Methods). Specifically, if the bat pitches its head to angles greater than +90° pitch (resulting in flipping from upright to inverted position), the toroidal azimuth still remains the same. Importantly, the upright and inverted positions are represented continuously, but can be distinguished according to the pitch angle: The outer surface of the torus (white) corresponds to all upright positions ($-90° < \text{pitch} < +90°$), whereas the inner part of the torus (grey) corresponds to all inverted positions ($+90° < \text{pitch} < +180°$ or $-180° < \text{pitch} < -90°$). **d**, Detailed depiction of two different azimuthal directions on the torus (shown as red and purple rings in **c**). Right panel (0° azimuth): for an upright bat facing east (0° azimuth, 0° pitch), any change of the pitch angle (red ring) will not change the toroidal azimuth, which will remain 0°. Left panel (180° azimuth): analogously, for an upright bat facing west (180° azimuth, 0° pitch), any change of the pitch angle (purple ring) will not change the toroidal azimuth, which will stay 180°. Note, that this set of positions, corresponding to 180° azimuth (purple ring), is mapped onto the opposite side of the torus, relative to the set of positions corresponding to 0° azimuth (red ring). Therefore, unlike the ambiguous representation of head direction in spherical coordinates (**a**, **b**), there is no ambiguity in the toroidal representation: each point on the torus describes a unique orientation of the bat, and defines not only its head direction in 3D, but also whether the bat is in the upright or in the inverted position. **e**–**j**, Example of construction of the toroidal representation and angular transformations of the 2D rate-maps for the inverted session, for one pure azimuth neuron. **e**, **f**, 2D directional rate maps for the upright session (**e**) and inverted session (**f**) computed initially in spherical coordinates. **g**–**i**, Angular transformations of the 2D rate map of the same inverted session (shown in **f**), done in order to represent it in toroidal coordinates: **g**, 180° shift in azimuth; **h**, flipping the pitch axis (to represent it continuously and allocentrically); **i**, both transformations together (that is, 180° shift in azimuth and flipping the pitch axis). For each of the maps in **f**–**i**, the value of the 2D Pearson correlation coefficient, *r*, of this map with the upright map in **e**, is also indicated. **j**, The toroidal representation is constructed by concatenating the 2D directional map of the upright session (shown in **e**) with the map of the inverted session after both transformations (shown in **i**). **k**, Difference in 2D correlations (Δ corr) of the firing maps in the upright and inverted sessions, before (**f**) versus after the various angular transformations (examples shown in **g**–**i**). Bars, various angular transformations (see panels **g**–**i**), which included shifting the azimuth of the inverted session by 180°, or flipping the pitch in order to represent it allocentrically, or both. Error bars, mean ± s.e.m.; $^{*}P < 0.05$. Comparisons are shown for pure azimuth cells (**k**, upper panel, $n = 84$ (42 cells × 2 sessions)), pure pitch cells (middle, $n = 14$), and conjunctive azimuth × pitch cells (lower panel, $n = 28$). Consistent with the toroidal model, a 180° azimuth-shift of the inverted map increased substantially the correlation with the upright-map for pure azimuth cells (**k**, upper panel-left bar; *t*-test, $P < 0.05$), but not for pure pitch cells (middle panel left bar: *t*-test, NS). Conversely, flipping the pitch increased substantially the correlation for pure pitch cells (middle panel middle bar; *t*-test, $P < 0.05$), but not for pure azimuth cells (upper panel middle bar: *t*-test, NS). For the azimuth × pitch conjunctive cells, both shifting the azimuth by 180° and flipping the pitch resulted in significant increase in correlation values (lower panel; *t*-test: $P < 0.05$, for all bars), as expected from cells encoding both azimuth and pitch. **l**, Similar analysis for azimuth × roll 2D maps did not show a significant effect of roll on the correlations between the upright and the inverted sessions, suggesting that the roll dimension is not crucial for 3D head-direction representation in bats. **m**, Population averages of 2D correlations of the firing maps in the upright versus inverted session, for all the head-direction cells, including azimuth, pitch and roll cells ($n = 156$ (78 cells × 2 sessions)), when represented in either spherical coordinates (left), or azimuth × pitch toroidal coordinates (middle), or azimuth × roll toroidal coordinates (right). These results suggest that an azimuth × pitch torus, but not the alternative models such as the sphere or an azimuth × roll torus, captures well the activity of head-direction cells in the bat presubiculum. Error bars, mean ± s.e.m.; $^{**}P < 0.01$; $^{***}P < 0.001$.

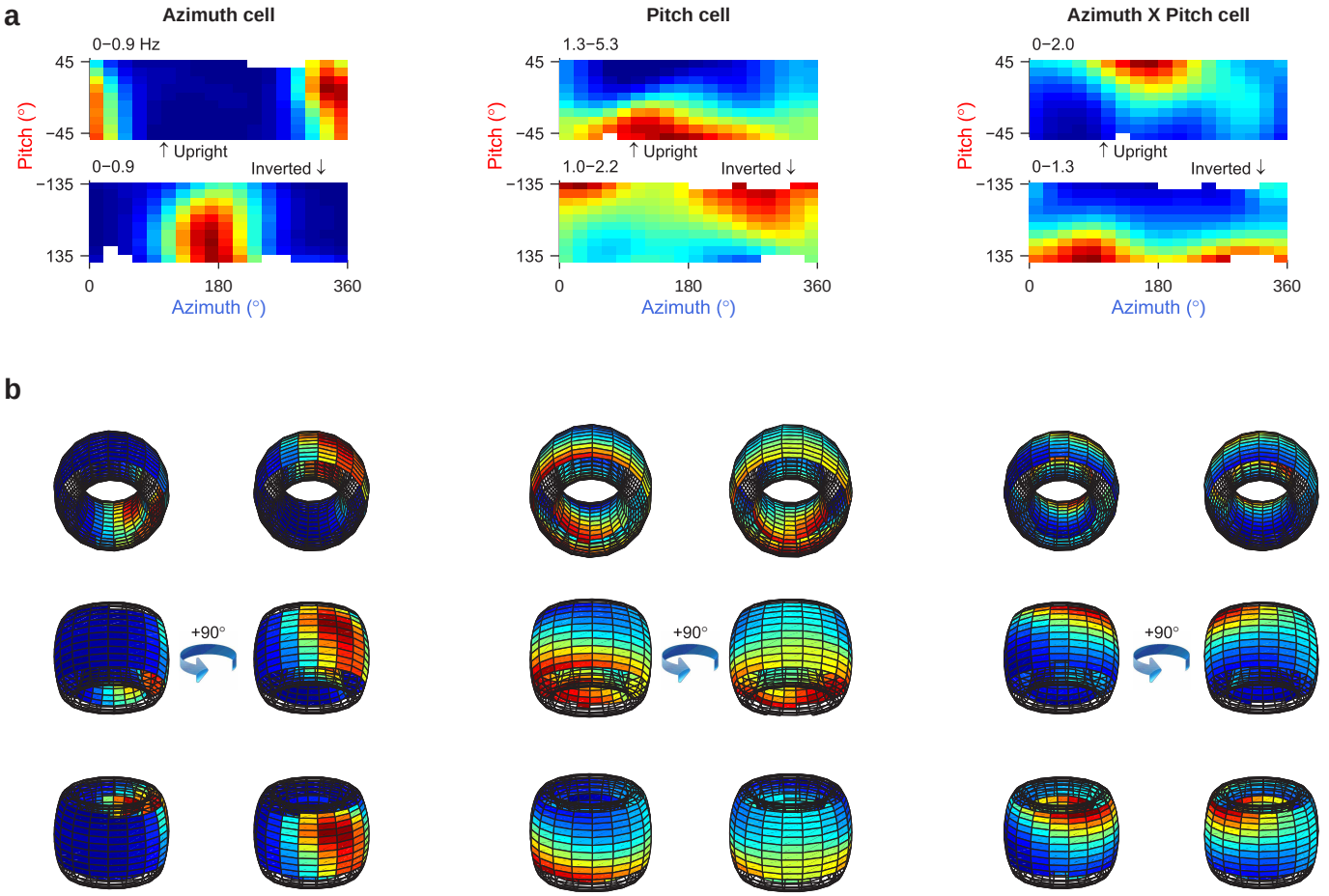

Extended Data Figure 8 | Toroidal representation of head-direction cells. **a**, 2D directional rate-maps of the upright (top) and inverted session (bottom), for a pure azimuth cell (left), pure pitch cell (middle), and a conjunctive azimuth × pitch cell (right) ; same neurons as in Fig. 3f of the main text. **b**, Same three cells as in **a**, shown in the toroidal representation from different viewing angles. Each cell is shown from two horizontal viewing angles (rotated 90° horizontally (azimuthally) with respect to each other) and from three different pitch viewing angles. The tori were constructed by plotting on the outside half of the torus the 2D directional rate map for the upright session, and on the inside half of the torus plotting the rate map of the inverted session in toroidal coordinates; see Extended Data Fig. 7e–i and Methods for the details of the angular transformations.

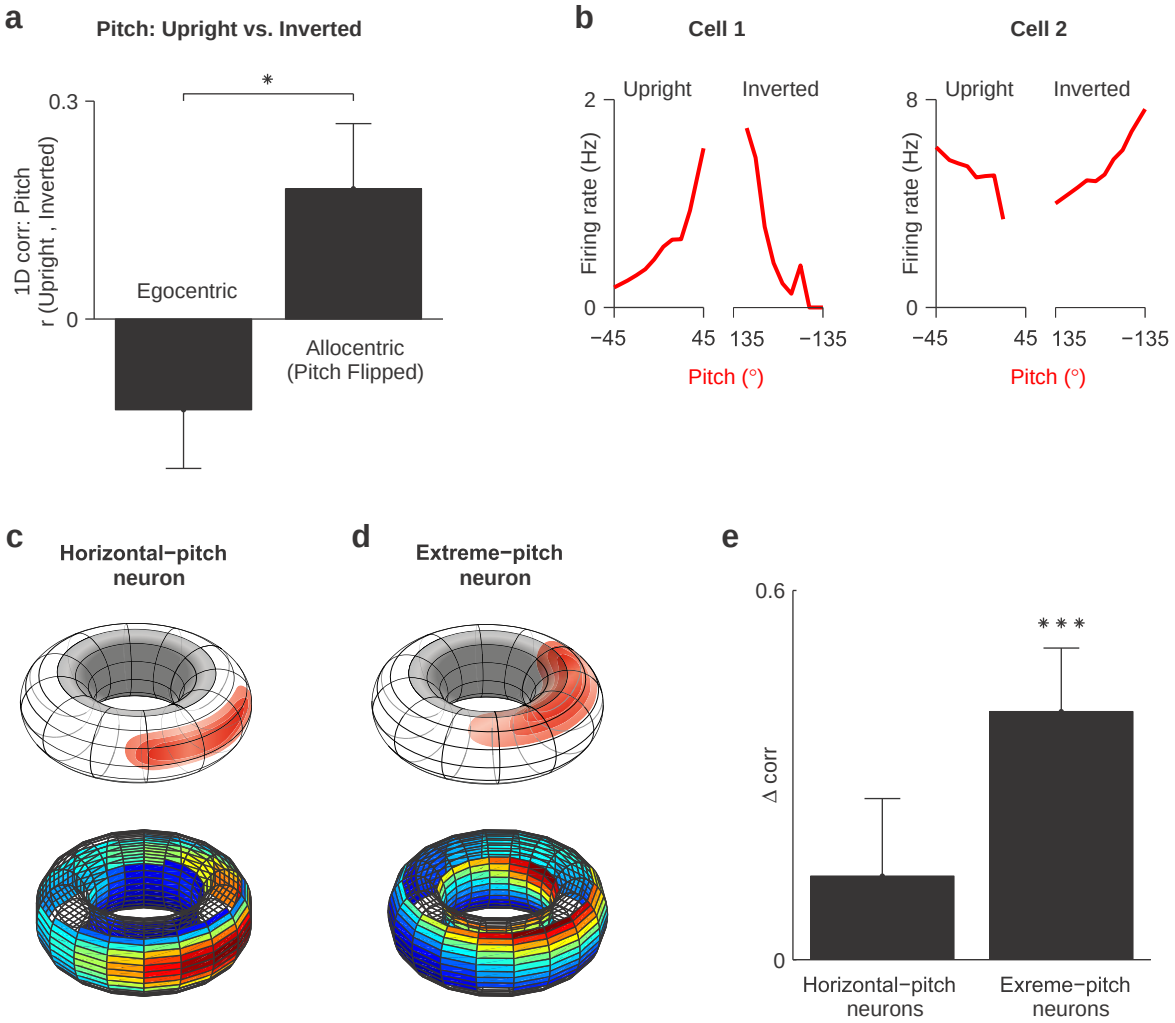

Extended Data Figure 9 | Torus topology predicts that tuning to pitch is allocentric and distinct between upright and inverted positions. **a**, According to the toroidal representation, pitch is computed in a world reference frame (allocentric) and not in body reference frame (egocentric). In the upright position, the two reference frames are indistinguishable. For example, when a bat pitches its head towards the moon (positive allocentric pitch) it also raises its head away from its chest (positive egocentric pitch). However, in the inverted position, allocentric head pitch is flipped with respect to the egocentric one. When the bat is upside-down and looks towards the moon (positive allocentric pitch), it now brings the head towards the chest (negative egocentric pitch). To test which of these reference frames is most consistent with our neural data, we computed the correlation between the pitch 1D tuning curves of the upright sessions versus the inverted session, in the two reference frames (for the experiments in setup number 1). Correlation of pitch tuning-curves between the upright and inverted positions was higher when the inverted session was plotted in allocentric coordinates ($n = 42$ (21 cells × 2) upright sessions; we included in the analysis only cells that were significantly tuned to pitch). *$P < 0.05$. **b**, A toroidal representation implies that pitch has a continuous representation, where every pitch angle corresponds to a unique orientation along a 360° ring of possible pitch angles (see Fig. 3d, red ring). This implies that if a neuron is active mostly at extreme pitch angles during the upright session ('extreme-pitch' neuron), it is likely to be active also at the contiguous pitch in the inverted session. Shown here are examples of two pitch cells with tuning to non-zero pitch angles in the upright session (cell 1, positive pitch; cell 2, negative pitch). 1D tuning to pitch is plotted for the average neuronal activity of the cell during the two upright sessions ('upright', left), and for the inverted session ('inverted', right). Note that the two cells exhibit contiguous firing in the inverted and upright sessions. **c**–**e**, The toroidal model generates a prediction, that such a continuity between the upright and the inverted session (as shown in **b**), should occur for cells tuned to 'extreme pitch' (see example in **d**), but not for cells tuned to horizontal pitch (example in **c**). More specifically, in the toroidal model, neurons with preferred pitch at around 0°, an angle at which the head of an upright bat is parallel to the ground ('horizontal pitch' cells), are not expected to fire when the bat is inverted with its head being parallel to the ground, because these two situations are topologically distinct in the toroidal but not in the spherical representation (Fig. 3d vs 3c and Extended Data Fig. 7d vs 7b). In contrast, neurons tuned to an extreme pitch angle in the upright position, are likely to fire to some extent also in the contiguous part of the inverted session, as the 'patch of activity' on the 'external side' of the torus (which corresponds to upright position) is likely to extend also onto the 'inner side' of the torus (corresponding to inverted position). Therefore, according to the toroidal (but not the spherical) model, the correlations between the upright and inverted sessions for cells tuned to 'extreme pitch' are expected to be higher than for cells tuned to 'horizontal pitch'. This prediction was tested here, and was indeed confirmed (see below). **c**, Upper panel, schematic representation of an azimuth × pitch cell, exhibiting pitch tuning to 0° (a 'horizontal pitch' neuron). Lower panel, example of an actual neuron exhibiting pitch tuning to 0°, similar to the schematic. Note that in both the schematic and in the real neuron, no directional field is present in the inverted session (that is, no firing on the inner (grey) part of the toroidal manifold), as predicted above. **d**, Upper panel, schematic representation of an azimuth × pitch cell, tuned to positive pitch (an extreme pitch neuron). Lower panel, example of an actual neuron exhibiting tuning to positive pitch, similar to the schematic. In this case, the activity of the neuron in the upright session is in fact correlated with its activity in the inverted session, as predicted above. **e**, Differences in 2D correlations between the upright and inverted session, for all the pitch-tuned neurons recorded in setup number 1 (both pure and conjunctive), computed similarly to the correlation analysis in Extended Data Fig. 7k (see Methods). This correlation was significantly larger for pitch cells that were tuned to extreme pitch (pitch ≤ −35° or pitch ≥ + 35°; 'extreme pitch', $n = 22$ cells × sessions), compared to pitch cells tuned approximately to zero pitch (between −35° and +35°; 'horizontal pitch', $n = 20$ cells × sessions). Error bars, mean ± s.e.m.; ***$P < 0.001$.

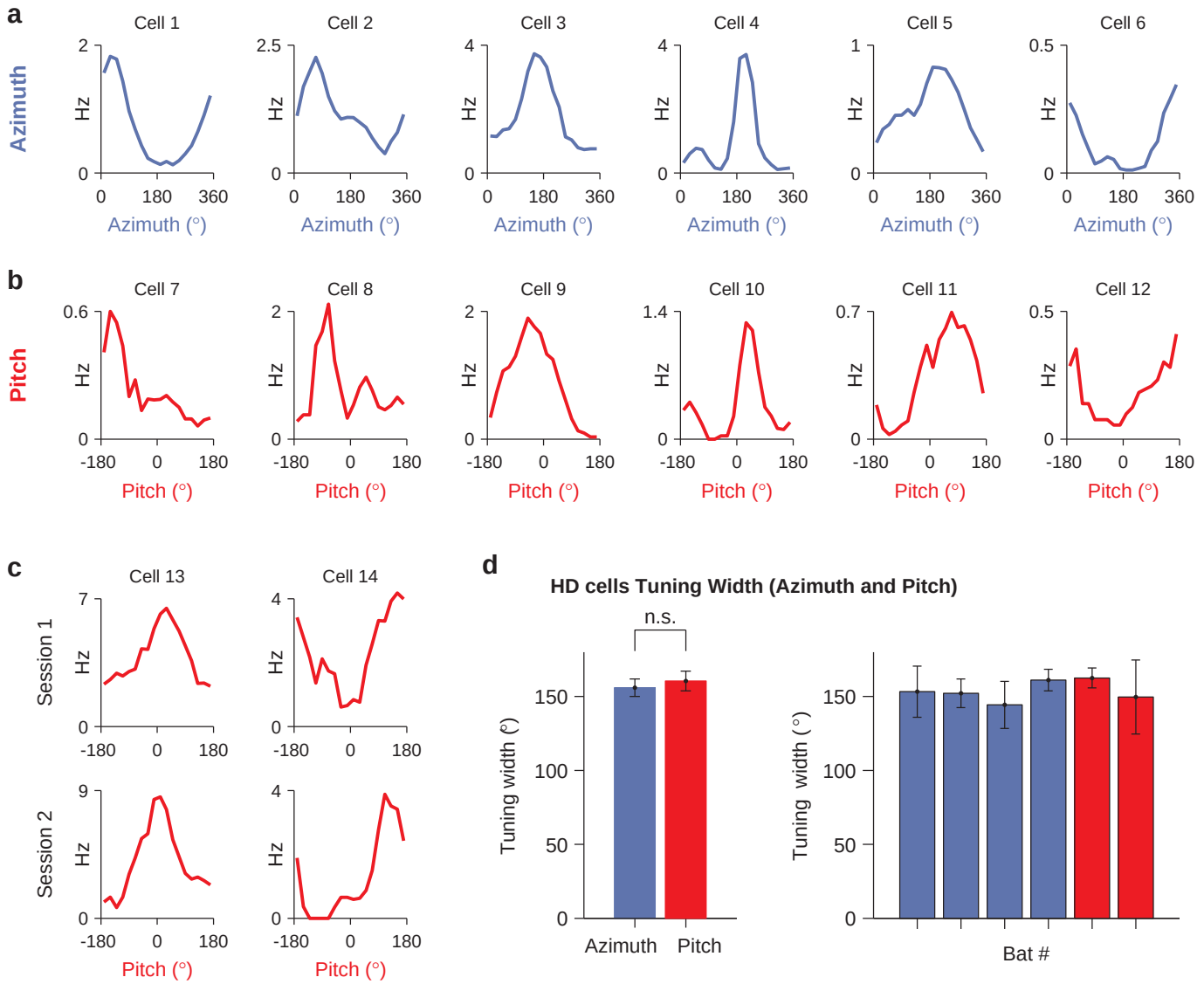

Extended Data Figure 10 | Pitch cells are narrowly tuned and span a range of 360°, similar to azimuth cells. **a**, **b**, Example azimuth cells recorded on the arena floor in setup number 1 (panel **a**) and pitch cells recorded on the vertical-ring in setup number 2 (panel **b**), showing that preferred directions of both neuronal types span the entire range of 360° (from 0° to 360° of azimuth for azimuth cells, and from −180° to +180° of pitch angles for pitch cells). Cells were sorted according to their preferred azimuth (top) or preferred pitch (bottom), highlighting the similarity of the tuning properties of azimuth cells and pitch cells. **c**, Pitch cells that were recorded on the vertical ring in two separate sessions exhibited a stable unimodal tuning. **d**, Tuning width to azimuth and to pitch. Left, population average tuning width. Right, average tuning widths for each individual animal (one bar per animal: azimuth, first 4 bars, coloured blue; pitch, last 2 bars, coloured red). The first 4 bars represent the tuning widths of azimuth cells recorded from the 4 bats in the upright-crawling experiment (setup number 1), and the last 2 bars represent the tuning widths of pitch cells recorded from the 2 bats in the vertical-ring experiment (setup number 2). Error bars, mean ± s.e.m.

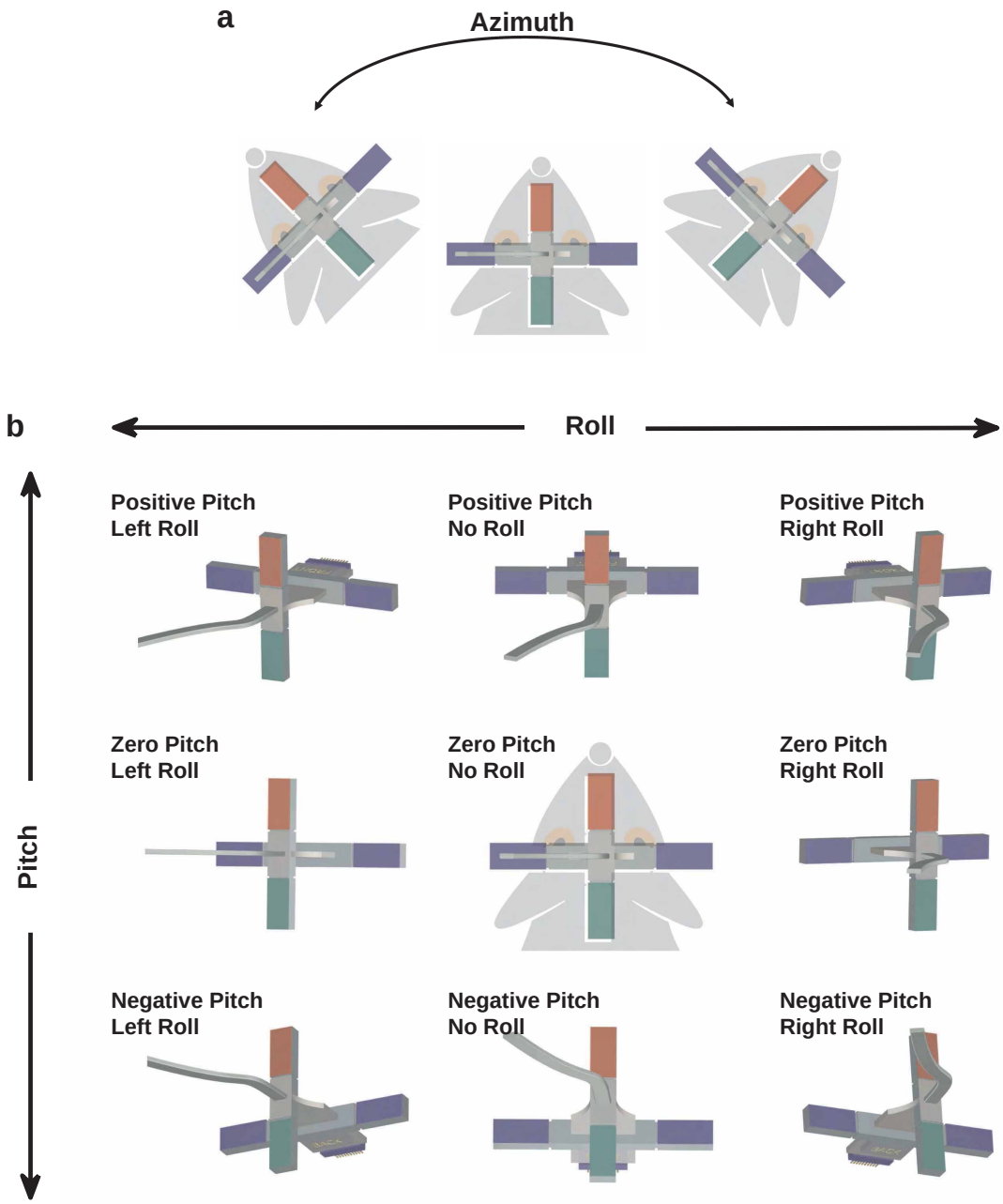

Extended Data Figure 11 | Device used for measuring the 3 Euler angles of the bat's head, based on a 3D non-coplanar arrangement of four LEDs. **a**, **b**, Schematic illustrations of the device used for computing the head-direction angles using the top-view camera. This device was mounted on the recording headstage, and allowed measuring the Euler angles using one overhead camera (Methods). Shown are several camera-views of a schematic illustration of the four-LED headstage, rotated in azimuth (**a**) or rotated at different combinations of pitch and roll (**b**). Central panels in both **a** and **b**: zero pitch and no roll ('flat head' position). The azimuth of the device was defined as the absolute direction of the red LED along the green–red direction. Pitch and roll were kept constant in all the plots in **a**; azimuth was kept constant in all the plots in **b**.

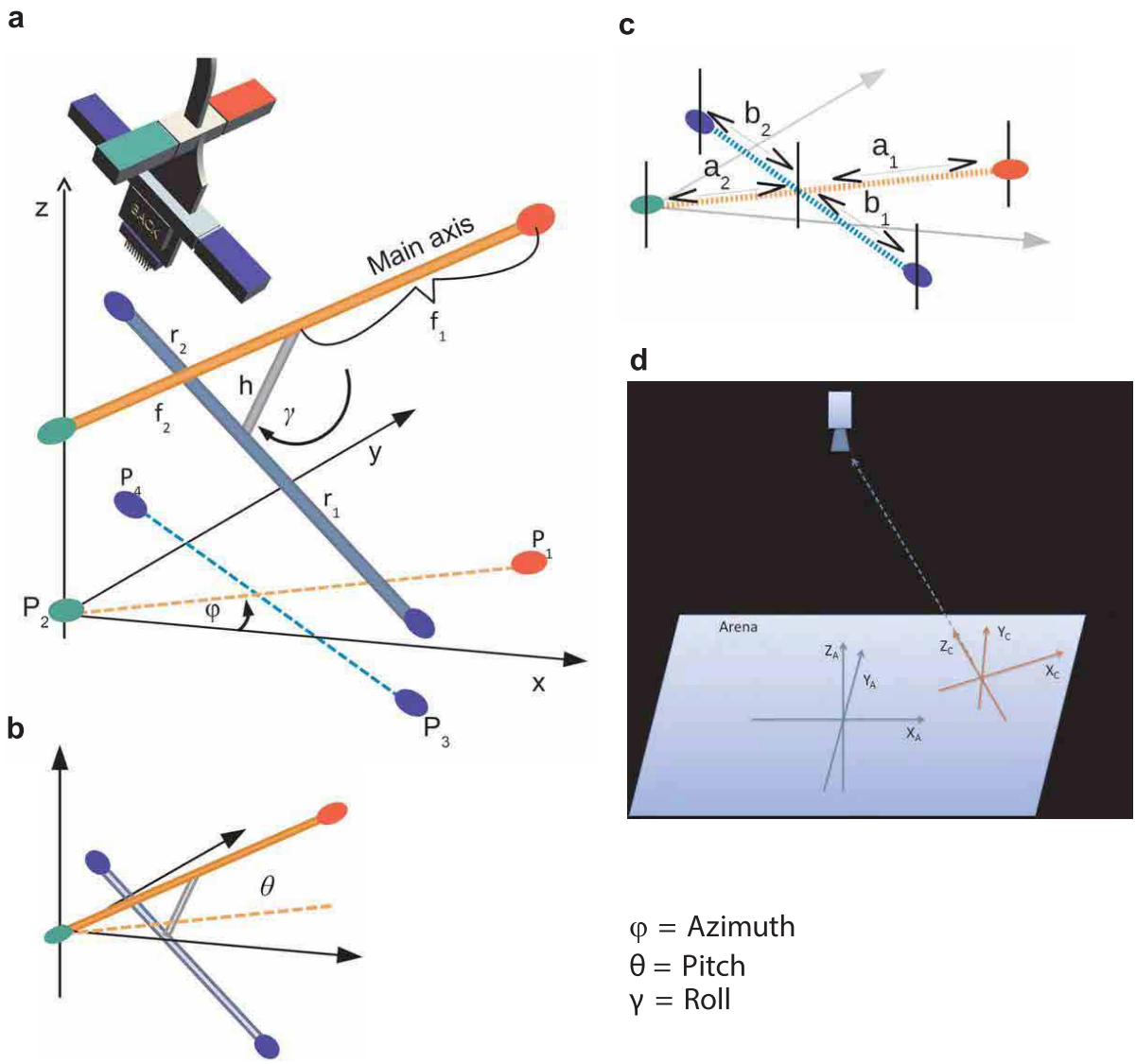

Extended Data Figure 12 | Definitions of intermediate angles used during the computation of the final Euler angles of the head. In order to compute the final Euler angles (in arena coordinates), we first computed intermediate Euler angles with respect to the plane of the camera, and then transformed them into arena coordinates based on the *x*–*y* position of the animal inside the arena (see Methods for the detailed computation and full definitions of these angles). **a**, **b**, Illustration of the 3D tetrahedral arrangement of 4 LEDs, including the relevant geometry and angles. **c**, Illustration of measurement as seen by the camera. The distances relevant for the measurement of angles have been labelled a_1, a_2, b_1, b_2. **d**, Coordinate frames of the arena ('$_A$') and camera-view ('$_C$'). Shown are the arena frame in blue and an example of the camera frame in red, for a particular location of the bat. Note that the alignment of the camera frame with respect to the arena frame changes as a function of the position of the LED device (position of the bat's head) within the arena; the algorithm described in the Methods section disambiguates these changes.